CARIB12: A Regional Community Earth System Model / Modular Ocean Model 6 Configuration of the Caribbean Sea

Giovanni Seijo-Ellis[1], Donata Giglio[1], Gustavo Marques[2], and Frank Bryan[2]

[1]Department of Atmospheric and Oceanic Sciences, University of Colorado Boulder, Boulder, CO, USA
[2]Climate and Global Dynamics Laboratory, U.S. National Science Foundation National Center for Atmospheric Research, Boulder, CO, USA

Correspondence: Giovanni Seijo-Ellis (giovanni.seijo@colorado.edu)

Abstract.

A new CESM/MOM6 ocean-only regional 1/12 ° configuration of the Caribbean Sea is presented and validated. The model configuration was developed as a response to the rising need of high-resolution models for climate impact applications. The configuration is validated for the period covering 2000-2020 against ocean reanalysis and a suite of observation-based datasets. Particular emphasis is paid to the configuration's ability to represent the dynamical regime and properties of the region across sub-seasonal, seasonal and inter-annual timescales. Near-surface fields of temperature, salinity and sea-surface height are well represented. In particular the seasonal cycle of sea-surface salinity and the spatial pattern of the low salinity associated with the Amazon and Orinoco river plumes is well captured. Surface speeds compare favorably against reanalysis and show the mean flows within the Caribbean Sea are well represented. The model reproduces known pathways and timing for river plume waters intruding the region. The seasonal cycle of the mixed layer depth is also well represented with biases of less than 3 m when comparing to ocean reanalysis. The vertical structure and stratification across the water column is represented favorably against ship-based observations with the largest simulated biases in the near-surface water mass and the sub-surface salinity maximum associated with the sub-tropical underwater mass. The temperature and salinity variability of the vertical structure is well represented in the model solution. We show that mean ocean mass transports across the multiple passages in the eastern Caribbean Sea compare favorably to observation-based estimates, but the model exhibits smaller variability compared to ocean reanalysis transport estimates. Furthermore, a brief comparison against a 1° CESM global ocean configuration shows that the higher resolution regional model improves significant biases in sea-surface salinity and mixed layer depth in particular. Additionally, the regional model better represents important features and variability within the Caribbean Sea compared to the 1° model. Overall, the regional model reproduces to a good degree the processes within the Caribbean Sea and opens the possibility of regional ocean climate studies in support of decision making within CESM.

1 Introduction

The Caribbean Sea (CS) is a crucial pathway for ocean circulation. Understanding the dynamics of the Caribbean Sea holds profound implications for global climate patterns (Schmidt et al., 2004; Restrepo et al., 2019; Gradone et al., 2023; Torres et al., 2023) and regional marine biodiversity (Miloslavich et al., 2010; Bowen et al., 2013; Chollett et al., 2012). The inflow to

the eastern CS is dominated by two sources: a) North Atlantic waters, and b) Tropical Atlantic waters modulated by the large freshwater runoff from the Amazon and Orinoco rivers (Johns et al., 2002; Coles et al., 2013; Hormann et al., 2015; Grodsky et al., 2015; Gradone et al., 2023; Seijo-Ellis et al., 2023). The transport of waters into the eastern CS (from here on referred to as inflow) via the passages along the greater and lesser Antilles exhibits variability across different time scales. At the daily to monthly time scales, the near-surface transport may be driven by surface winds (Johns et al., 2002; Andrade-Amaya, 2000) and/or particular river plume events (Seijo-Ellis et al., 2023). The interactions between topography (along the islands in the eastern CS) and density fronts of plume waters result in baroclinic instabilities that often develop into mesoscale eddies that transverse the CS (Andrade and Barton, 2000; Southwick et al., 2016). At the seasonal scale, the near-surface transport and salinity of the CS are dominated by the runoff from the Amazon and Orinoco river plumes peaking in boreal spring and reaching its minimum in early fall (Corredor and Morell, 2001; Johns et al., 2002; Jouanno et al., 2012; Seijo-Ellis et al., 2023). At inter-annual to longer timescales, the flow and properties of the waters entering the eastern CS may be modulated by large scale modes of variability such as the El Niño Southern Oscillation and the Atlantic Meridional Mode via coupled processes between the atmosphere, land and ocean (Restrepo et al., 2014; Arias et al., 2015; Restrepo et al., 2019). Below 100-150 meters, the inflow is modulated at inter-annual and longer time scales and is an important component of the Atlantic Meridional Overturning Circulation (AMOC) return flow (Wilson and Johns, 1997; Johns et al., 1999, 2002). The transport includes water masses such as Sargasso Sea Water, Subtropical Underwater, Antarctic Intermediate Water, South Atlantic Water, and North Atlantic Deep Water (Corredor and Morell, 2001; Johns et al., 2002; Seijo-Ellis et al., 2019; Gradone et al., 2023). Recent studies suggest that the deep transport of South Atlantic Waters through the Anegada Passage may be larger than originally estimated (Gradone et al., 2023). These studies indicate that the inflow of waters to the Caribbean Sea is an important component towards understanding changes to the AMOC under a changing climate (Bryden et al., 2005; Frajka-Williams et al., 2019; Caesar et al., 2018).

The Amazon and Orinoco river plumes are also responsible for variability within the Caribbean Current via the generation of vertical shear (Chérubin and Richardson, 2007) that accelerates its mean flow. In addition, the strong near-surface stratification due to the plumes limits vertical mixing and can have important implications for the formation and evolution of tropical storms in the CS by modulating heat fluxes and exchanges with the atmosphere (Godfrey and Lindstrom, 1989; Lukas and Lindstrom, 1991; Rudzin et al., 2017). While the inflow modulates temperature and salinity variability in the CS, there are other important local processes that contribute to upper ocean variability in the basin. For example, tides across the CS drive local vertical mixing and enhance primary productivity (Kjerfve, 1981; Giese et al., 1990; Sosa, 2001; Ezer et al., 2011) in different areas within the CS. Alongshore winds drive upwelling along the southern CS via Ekman transport (Andrade-Amaya, 2000; Digna et al., 2018) and mesoscale eddies can lead to the formation of thermohaline staircases and mixing via double-diffusion (Morell et al., 2006).

Studying these processes for the present day is a relatively straightforward endeavor combining observations and regional ocean models, but at climate scales additional challenges may arise (Ezer et al., 2011; Solano et al., 2018; Mukherjee et al., 2023; Seijo-Ellis et al., 2023). Coupled climate models have been able to reproduce past and present trends in the Earth System becoming a powerful tool to examine mechanisms and future changes (Hurrell et al., 2013; Meehl et al., 2014; Kay et al.,

2015). Nevertheless, the low spatial resolution does not allow to resolve processes at fine scales, and the dependency on model parameters result in uncertainties across models and against observations (Tebaldi and Knutti, 2007; Hourdin et al., 2017). For example, the typical horizontal resolution for the ocean component in coupled climate models is of 0.25° or coarser, which does not resolve the numerous passages in the eastern CS, nor the processes that are so intrinsically connected to the topography and geography of the region. Furthermore, certain longstanding biases in climate simulations can often be traced to the ocean component of the coupled model because important oceanic processes are unresolved (or poorly represented) resulting in biases in ocean heat fluxes, air-sea fluxes, and gradients along temperature and density fronts (Large and Danabasoglu, 2006; Kirtman et al., 2012; Danabasoglu et al., 2014; Roberts et al., 2016). More recently, Richards et al. (2021) show that changes in the mixed layer depth and buoyancy fluxes under climate change may result in reduced submesoscale activity which, even in the presence of appropriate parameter tuning, may be an additional source of biases in the ocean for climate projections. While there is a rising need for regional climate research to inform decision making, the shortcomings of global climate models make them unsuited for these purposes. Thus, dynamically downscaling ocean climate projections using a high-resolution ocean model is an enticing proposition to properly examine regional ocean impacts under a changing climate (Chamberlain et al., 2012; Brickman et al., 2021; Richards et al., 2021).

The Community Earth System Model 2 (CESM, Danabasoglu et al. (2020)) uses the Parallel Ocean Program (POP) 2 as its ocean component. However, the Modular Ocean Model 6 (MOM6, Adcroft et al., 2019) is set to replace POP in future versions of CESM. Meanwhile, MOM6 has been made available to users in release versions 2.2 and higher of CESM2. MOM6 uses innovative approaches that make it an ideal model for high resolution configurations at the regional and global levels. For example, the use of the Arbitrary Lagrangian-Eulerian (ALE) method allows for the use of several different vertical coordinate systems (geopotential, isopycnal, terrain-following or hybrid), making the model adaptable to the specific constraints of the topography of a region and purposes of the configuration. The model can be run in fully coupled global configurations within CESM, as well as in ocean-only, and other supported combinations. In addition, it provides the user the ability to dynamically downscale the ocean component in global simulations while remaining within the CESM framework. As a first step towards this goal, here we present an ocean only CESM/MOM6 configuration of the Caribbean Sea. This configuration (here on referred to as CARIB12) was developed to understand present and future variability of the near-surface Caribbean Sea waters. This paper focuses on the configuration of the model and a thorough validation for the present day period (2000-2020) as a benchmark for upcoming future climate projections. In Section 2 we describe the model configuration in detail and, the datasets and methods used to validate the model. The validation and results are shown in Section 3 and conclusions are presented in Section 4.

2 Data and Methods

2.1 Model Description

The CARIB12 configuration is built on a horizontal Arakawa C-grid (Arakawa and Lamb, 1977) at 1/12 ° resolution ($\approx$ 9 km) resulting in 759 x 457 tracer points. The grid extends from -6°S to 32°N and from -35.5°W to -98.5°W (Figure 1a). The Pacific Ocean is masked to eliminate an unnecessary open boundary and improve computational efficiency. The topography (Figure

1a) was generated using the Shuttle Radar Topography Mission 15+V2.1 dataset (Tozer et al., 2019) and was smoothed using a Cressman weighted interpolation scheme. Manual edits were made to the land-ocean mask and topography to ensure proper width and depth of the numerous passages between the Caribbean islands, the Amazon river delta, and along the coastline in general. In the vertical, a 65 layer z* (z-star, Adcroft and Campin, 2004) grid is used with a maximum spacing of 2.5 m at the surface and increasing grid spacing at depth using a hyperbolic tangent function (to a maximum spacing of 248.7 m above the maximum depth of 6500 m).

CARIB12 uses a baroclinic time step of 900 s and a thermodynamic time step of 1800 s. The background kinematic viscosity of the interior is set to $1 \times 10^{-6} \frac{m^2}{s}$. CARIB12 uses a Smagorinsky horizontal viscosity with a Smagorinsky constant of 0.02 and a bi-harmonic viscosity set to $5 \times 10^8 \frac{m^4}{s}$. The configuration of the horizontal viscosity was determined after exploring different options and combinations within MOM6, including the use of a Laplacian viscosity and different values for the corresponding constants. The final configuration was largely determined by the mean flows into the CS across the multiple passages between the Caribbean Islands, recognizing the importance of these flows in driving processes and variability within the CS. Vertical mixing is specified via the CvMix library (Griffies et al., 2015) with a background diapycnal diffusivity of $1 \times 10^{-6} \frac{m^2}{s}$. CvMix utilizes the K-Profile Parameterization (KPP) of Large et al. (1994) for the boundary layer parameterization, mixing due to double-diffusion and shear-driven turbulence. The parameterization of Fox-Kemper et al. (2011) is implemented for the re-stratification of the mixed layer by sub-mesoscale eddies with a front length scale of 1500 m. Additional details of the physical configuration and choice of parameterizations in CARIB12 are given in the following subsections and summarized in Table 1.

The CARIB12 configuration has several key differences with other recent MOM6 configurations that cover a similar region, like the NWA12 configuration of Ross et al. (2023). For instance, the coupling infrastructure used in CESM-MOM6 is the Community Mediator for Earth Prediction Systems (CMEPS), whereas NWA12 uses the Flexible Modeling System (FMS) coupler. In terms of the physical configuration, a few distinctions are worth highlighting. The vertical mixing parameterizations are entirely different. As CARIB12 is a CESM-MOM6 configuration we use KPP for the boundary layer mixing parameterization which is the same scheme used in CESM (Large et al., 1994; Danabasoglu et al., 2020). On the other hand, NWA12 uses the energetics based Planetary Boundary Layer (ePBL) scheme of Reichl and Hallberg (2018). Vertical mixing in CARIB12 is specified via the CvMix library which parameterises vertical mixing in the interior using schemes that are different to those in NWA12 (Griffies et al., 2015). For example, shear-driven mixing in CARIB12 is handled by the parameterization of Large et al. (1994), whereas NWA12 applies the Jackson et al. (2008) scheme.

2.1.1 Initial and Open Boundary Conditions

Initial conditions are prescribed from the GLORYS12V1 reanalysis (GLORYS12, Jean-Michel et al., 2021). The GLORYS12 data is on a 1/12° resolution grid with 50 vertical levels. The model grid has two open boundaries, one to the east, one to the north (Figure 1a). The open boundary conditions are specified daily using temperature, salinity, sea-surface height (SSH), meridional (v) and zonal (u) velocity components from GLORYS12. Ten tidal constituents are specified at the boundaries with tidal potential forcing included as a body force in the momentum equations. The tidal amplitudes and phases were obtained from the TPXO Global Tidal Model 9v5a (Egbert and Erofeeva, 2002). Effects of self-attraction and loading are accounted for

using the scalar approximation of Accad and Pekeris (1978) with a coefficient of 0.094. The barotropic flow at the boundaries is treated with a Flather boundary condition (Flather, 1976). The baroclinic component is specified using the Orlanski (1976) boundary condition. The boundary flows are nudged to exterior velocities at timescales of 0.3 days for inflow and 360 days for the outflow. Nudging layers for temperature, salinity and velocities are applied to minimize noise at the boundaries that may contaminate the interior. The layers are based on mean monthly fields from GLORYS12. Damping in the nudging layers decays across 15 grid points away from the boundaries (dashed white lines in Figure 1a) with maximum damping applied at the boundary grid cells. Damping at each point i is given by: $damping_i = \frac{1}{dmin+dr*i}$, where $dr = (dmax - dmin)/(npts + 1)$, $dmax = 20$ days, $dmin = 2$ days and $npts = 15$ (corresponding to the number of points across which damping decays). The resulting equivalent restoring time from the applied nudging is in order of 10 days (at the boundaries) and 150 days at the farthest specified point from the boundary). The parameters for the applied damping were determined as a balance between reducing noise at the open boundaries and not influencing the solution towards the center of the domain. In general, low resolution climate simulations, like those that will be downscaled using CARIB12, do not have high-frequency mesoscale variability that would be drastically attenuated by the applied nudging. Furthermore, the nudging will help prevent the formation of artificial currents and temperature/salinity signals along the boundaries. Nevertheless, as with any model, the nudging layers and other parameters might need to be revisited depending on the climate simulation being downscaled.

2.1.2   Additional Forcings

The atmospheric forcing is prescribed from the Japanese 55-year reanalysis (JRA55-do, Tsujino et al., 2018) and is specified every 3 hours. Surface air temperature, downwelling shortwave radiation, downwelling longwave radiation, zonal and meridional wind, specific humidity, sea-level pressure, and precipitation all referenced to 10 m above sea-level in combination with SST and surface velocities are used to compute surface fluxes of heat, water and momentum using the Large and Pond (1981) bulk formula. The JRA55-do was developed following the Ocean Modeling Intercomparison Project protocol, and is also used for many of the CESM simulations that will be downscaled with CARIB12. Freshwater runoff input is generated using the Global Flood Awareness System (GloFAS, Zsoter et al., 2021). The CESM Climatological Data River model was modified to use with the GloFAS data. The daily runoff is specified every 3-hours with the atmospheric forcing and is spread horizontally across a maximum radius of 600 km radius from the grid point the runoff is prescribed with an e-fold scale of 200 km. The maximum radius for the spreading and the e-fold scale were determined through an ad-hoc process by testing different combinations of these parameters. The combination specified here resulted in improved biases in salinity. A monthly climatology of surface Chlorophyl-a (Chl-a) is provided from the SeaWIFS satellite mission (NASA Ocean Biology Processing Group, 2018) for the Manizza et al. (2005) opacity scheme.

2.2   Validation datasets

For the model validation we use several datasets. These include the same GLORYS12 Ocean reanalysis (Jean-Michel et al., 2021) used for the open boundaries and for the initial conditions. The reanalysis uses the CORAv4.1 database (Cabanes et al., 2013) to assimilate observations of sea-level anomalies, sea surface temperatures (SST), and *in-situ* profiles of temperature

and salinity from Argo floats (Argo, 2000), shipboard XBT and CTD. Daily fields of temperature, salinity, mixed layer depth (MLD), sea-surface height (SSH) and velocities are used to validate CARIB12. Additionally we validate the mixed layer depth (calculated using the $\Delta 0.03 \frac{kg}{m^3}$ density criterion) with the climatology of de Boyer Montégut et al. (2004). Altimetry derived geostrophic currents with Ekman flow corrections from modeled fields from the GLOBCURRENT product (Rio et al., 2014) are used to validate the surface velocities and eddy kinetic energy field. The eddy kinetic energy was calculated as follows:

$EKE = (\frac{1}{2})(u'^2 + v'^2)$, where u' and v' are velocity anomalies resulting from decomposing the velocities into a mean velocity ($\overline{u}$ and $\overline{v}$) and the anomaly: $u = \overline{u} + u'$.

Further validation is done for sea-surface temperature (SST) fields against the Optimum Interpolation SST dataset (Huang et al., 2021) and, for sea-surface salinity (SSS) fields, against the Multi Observation Global Ocean Sea Surface Salinity product (Droghei et al., 2016). The errors associated with the Multi Observation Global Ocean Sea Surface Salinity product used here are quite small (in the order of 10^{-3}) even along the coastlines which provides a good baseline for our validation. The SST, SSS and MLD are also compared to the $1°$ resolution CESM-POP configuration used for the Ocean Model Intercomparison Project phase 2 (Tsujino et al., 2020).

We have additionally validated water mass representation in the model against ship-based observations (CCHDO Hydrographic Data Office, 2023), using the Argovis application programming interface (Tucker et al., 2020) to identify WOCE lines within the region of interest (i.e. WOCE lines A20 and A22, Figure 1b) and specific cruises within the time frame of the simulation (2000-2020). Profiles of temperature and salinity corresponding to the closest profile in time and space to each ship-based profile were extracted from the CARIB12 solution and the GLORYS12 reanalysis. The cruise profiles, CARIB12 and GLORYS12 profiles were binned in 0.2 PSU $\times$ 1°C bins after being vertically interpolated onto a common grid to generate joint probability functions of Temperature-Salinity diagrams for each dataset. A total of 250 profiles from the following cruises are used in the analysis presented here: 43 profiles from 35A3200304, 43 profiles from 316N200309, 71 profiles from 316N200310, 43 profiles from 33AT20120324, and 50 profiles from 33AT20120419.

When comparing our model to different data products, the dataset with higher resolution was bi-linearly interpolated onto the horizontal grid of the product with lower resolution using the xESMF Python Package (Jiawei Zhuang et al., 2023). The CARIB12 solution was also saved at run-time on the GLORYS12 vertical grid and the ship-based profiles were re-gridded onto that same vertical grid. As this configuration has been developed for dynamical downscaling of climate simulations, validating seasonal to interannual variability is the target benchmark and the overall validation focuses on these time scales. A summary of the validation datasets and relevant information is included in Table 2.

3 Results

3.1 Near-surface Fields

In the following subsections we examine temperature, salinity, sea level and kinetic energy in the shallowest layer of the model ($0 - 2.5$ meters) within the domain of interest (the region shown in 1b), as described in Section 2. Our focus is on time averaged fields, with the average computed for the full time series or specific seasons.

3.1.1 Temperature and salinity

Within the domain of interest (Figure 1b), CARIB12 has a mean surface temperature of 27.5 °C with a spatial standard
deviation of 0.52 °C (Figure 2a). The spatial patterns of temperature across the domain are well represented and CARIB12
captures the upwelling system in the southern CS. The GLORYS12 reanalysis mean SST is 27.6 °C with a standard deviation of
0.56 °C (Figure 2b). These statistics indicate good agreement and similar distributions between CARIB12 and the GLORYS12
reanalysis, with a small cold mean spatial bias of -0.15 °C (Figure 2c). The OISST data has a mean SST of 27.6 °C and standard
deviation of 0.55 °C (Figure 2d). CARIB12 shows biases against OISST similar to those in the comparison to GLORYS12, the
mean bias is -0.15 °C being dominated by biases in shallow areas and within the CS (Figure 2e).

CARIB12 compares favorably against both datasets not only in terms of time mean, but also for seasonal changes: corre-
lation very close to one is found between the CARIB12 12-month climatology and the 12-month climatology based on other
products (Figure A1); also, differences between the CARIB12 standard deviation for the 12-month climatology and the stan-
dard deviation in other products are generally within ≈ 10% of the values in the products used for validation (Figure A2).
The low resolution CESM-POP simulation represents the broad patterns and mean SST within the region of interest (Table 3).
However, it lacks proper representation of the extent and magnitude of features characteristic of the CS such as for example,
the magnitude of the upwelling system off the coast of South America (Figure A3a).

The spatial patterns of SSS in different seasons are consistent between CARIB12 and both GLORYS12 and the MOGO
observational dataset (Figures 3). Figure 3a-3e shows the mean winter (DJF) SSS for CARIB12 and the validation datasets:
the spatial mean in CARIB12 is 35.86 PSU with a mean bias of 0.14 PSU compared to GLORYS12 (Figures 3a and 3c), and a
bias of 0.05 PSU compared to the MOGO observational dataset (Figure 3e). Notably, GLORYS12 appears to have a freshwater
source in the region of the Dominican Republic and Puerto Rico resulting in positive biases within the CS. This is highlighted
by the red contour line corresponding to 35 PSU, shown in Figure 3b. During the summer (JJA), CARIB12 shows a mean bias
of 0.17 PSU compared to GLORYS12 and one of -0.12 PSU compared to MOGO (Figure 3j). The 35 PSU contour line (red
line in Figure 3) delineates the fresh water salinity front (based on the discussion in Seijo-Ellis et al., 2023) and shows that
the spread and extent of the plume waters is similar between CARIB12 and GLORYS12, but is much smaller in the gridded
observations (particularly during the winter, Figure 3a - 3e).

The seasonal spread of the low salinity plume from the Amazon and Orinoco rivers is well captured with peak high salinity
during the winter months within the CS and minimum salinity during the summer months (Figure B2a). The largest biases in
SSS are the areas of major riverine inputs: the Amazon and Orinoco rivers. These biases may arise from the specification of
the river runoff to the ocean and how mixing of the freshwater input in the ocean is handled in CARIB12 (and e.g. differences
with the corresponding choices in GLORYS12). In CARIB12, runoff is not distributed vertically in the ocean but rather spread
horizontally across a maximum radius of 600 km with an e-fold decay scale of 200 km at the shallowest layer. Also, some of
the large biases when comparing to observations may arise due to limited observations in the shallow shelf regions and the
interpolations done to grid the data. Nevertheless, the seasonal SSS is well represented in CARIB12 with good correlations

between datasets and smaller biases within the Caribbean Sea away from riverine sources. Known pathways of Amazon river waters into the CS are well reproduced as evidenced by a backtracking experiment (see Appendix B).

The smallest biases are generally found within the CS which indicate CARIB12 is performing well within the region of interest. Correlation close to one is found between the CARIB12 12-month climatology and the 12-month climatology based on other products, in most of the domain (Figure A4); also, within the CS, differences between the CARIB12 standard deviation for the 12-month climatology and the standard deviation in other products are generally within $\approx 25\%$ of the values in the products used for validation, except in the western part of the basin (Figure A6).

In contrast to the well simulated variability of SSS in CARIB12, the low resolution CESM-POP simulation exhibits biases that hinder the model's performance to properly represent the SSS variability within the Caribbean Sea (Table 3 and Figure A3b and A3c). There is an overall positive salinity bias irrespective of the season and the extent and magnitude of the Amazon and Orinoco river plumes are not well represented. These biases may be a product of several factors: biases in the specification of the river runoff, inadequate representation of sub-grid scale process and mesoscale eddies that play an important role in the spreading of the river runoff and salinity variability in the region, and/or biases inherent to the low resolution of the model.

3.1.2 Surface currents speed, eddy kinetic energy and sea surface height

The mean winter and summer surface speed is shown in Figure 4. The direction and spatial distribution of the near-surface flows is well represented in CARIB12 compared to GLORYS12 and the GLOBCURRENT product (arrows in Figure 4). The mean winter speed in CARIB12 is 0.19 m/s which corresponds to a mean bias of ≈ 0.02 m/s below the mean speed in GLORYS12. Compared to the GLOBCURRENT product, biases are overall larger with a mean negative bias of 0.07 m/s. The biases are within the same order of magnitude during the summer and show overall similar structures to the biases during the winter (Figure 4).

The largest biases during both seasons when compared to GLORYS12 occur along the region southwest of Hispaniola where two jets converge: the main Caribbean Current and the jet around $18°N$ (Chérubin and Richardson, 2007). The biases in this area are in the order of up to ≈ 0.12 m/s. This region is one of increased shear with rapidly varying bottom topography. Thus, difference in the topography between the models and the specification of the horizontal viscosity may be driving these biases. The speed compares well elsewhere in the region of interest including the narrow passages in the eastern CS. This indicates that CARIB12 represents well the inflow to the CS and the flows associated with the advection of the freshwater plumes from the Amazon and Orinoco rivers. The biases are larger when comparing CARIB12 to the altimetry and model based GLOBCURRENT (Figure 4e and 4j), but it is worth noting the difference in spatial resolutions and that the correction for Ekman flows is model based which may have its own biases for a small and under-sampled region like the CS. This is a worthy distinction because surface Ekman currents can reach 0.5 m/s in parts of the Caribbean Basin (Andrade-Amaya, 2000). The seasonal variability of the flow speed is well represented in CARIB12 with higher mean speeds in the summer and the lowest mean speeds during the winter, and this is evidenced by the eddy kinetic energy fields (Figure 5). In particular, CARIB12 captures the strengthening of the Caribbean current during the boreal summer months (JJA) as well as the re-circulation that occurs within the Colombian basin.

The seasonal eddy kinetic energy (EKE) for CARIB12, GLORYS12 and from the GLOBCURRENT product is shown in Figure 5: an overall mean negative bias is observed irrespective of the season and is most notable in the summer, when EKE is larger (Jouanno et al., 2012). These biases are particularly noticeable south of Hispaniola and in the southwest corner of the CS where a re-circulation of the surface flow occurs. Despite the lower EKE, seasonal variability is well represented in CARIB12 and the spatial variability compares well with GLORYS12 and the altimetry derived product (Figure 5c-5e). The seasonal increase in EKE during summer months is captured, although mesoscale patterns are not well represented. In particular, the increase in EKE extending westward across the Caribbean Sea (65° to 80° W) is not as strong in CARIB12 as GLORYS12 and the GLOBCURRENT product suggests. The 20 year time-mean EKE biases (not shown) are of the same order of magnitude as the seasonal EKE biases which indicate that the seasonal biases are dominated by biases in the long term mean. Further improvements in parameter choices may help reduce some of these biases and improve representation of mesoscale variability.

Figure 6 shows the winter and summer mean SSH anomalies (SSHa, spatial mean removed) for CARIB12 and GLORYS12. The winter mean SSHa in CARIB12 is -0.002 m and compares well with the mean in GLORYS12 (Figure 6a-c); similarly, a good comparison is seen for the summer (Figure 6d-f). The difference in both seasons indicate an overall more positive SSHa in CARIB12. The regions of positive biases in surface speeds (Figure 4) correspond to regions where the horizontal SSHa gradient is stronger in CARIB12, and viceversa where the biases in speed are negative (for example, southeast of Hispaniola around 16°N and 75°W). The SSHa within the region of interest is characterized by a negative SSHa structure along the shelf waters of South America whose meridional gradient delineates the location of the Caribbean Current. The meridional extent of this feature extends further off-shore in CARIB12 indicating a wider Caribbean Current in CARIB12 compared to GLORYS12. The standard deviations and correlations (Figure 6) show reasonable consistency between the solutions CARIB12 and GLORYS12. CARIB12 also reproduces well the seasonality of SSHa, with stronger meridional gradients and variability during the boreal summer compared to winter driving the intensification of the surface flows as described before. This seasonal cycle is also intrinsically connected to the seasonal variability of SSS (driven by the freshwater plumes of the Amazon and Orinoco rivers).

3.2   Mixed layer depth

We compare the winter and summer mixed layer depth (MLD) against the GLORYS12 reanalysis and the climatology by de Boyer Montégut et al. (2004). As detailed in Section 2, the calculation is done using the $\Delta 0.03\ kg/m^3$ density criterion with respect to surface values. CARIB12 compares favorably against GLORYS12 (Figure 7). The mean bias in the winter is 2.5 m, indicating an overall deeper MLD in CARIB12, with a RMSE of 6.31 and correlation of 0.89. In the summer, CARIB12 has a slightly shallower MLD than GLORYS12, with a mean bias of -0.13 m, RMSE of 3.71 and correlation of 0.89. The biases within the Caribbean Sea and away from the vicinity of the Amazon and Orinoco rivers are attributable to the small biases described for salinity: an overall positive salinity bias (Figure 3) corresponds to saltier waters in the near surface which leads to weaker vertical stratification (Figure 9) in the upper 0-100 m resulting in a deeper mixed layer particularly during the winter. In both seasons, the mean MLD from CARIB12 is closer to the mean of the de Boyer Montégut et al. (2004) climatology than

GLORYS12. A likely contributor to this improvement could be the added effect of tides in CARIB12 driving vertical mixing, a process that is not included in GLORYS12.

When comparing the MLD against the de Boyer Montégut et al. (2004) climatology, CARIB12 has an overall shallower MLD across seasons. During the winter, the mean MLD bias is -5.24 m, with a RMSE of 9.53 and correlation of 0.78. During summer, the bias is -6.58 m, with a RMSE of 8.03 and correlation of 0.83. CARIB12 represents well the MLD seasonality across the domain: the mixed layer is deepest in winter and becomes shallower during the spring as temperatures rise and the Amazon and Orinoco river plumes influence the Caribbean region. The mixed layer is overall shallowest during the summer months before deepening again in the fall as near-surface temperatures decrease and salinity increases in the absence of the Amazon and Orinoco river plumes. Overall, CARIB12 captures both the seasonal variability and spatial patterns of the MLD and compares well to GLORYS12.

The CESM-POP simulated MLD shows biases in the order of 13 m during the summer and 30 m during the winter for the mean MLD (Table 3 and Figure A3d-A3e). These biases in CESM-POP could be in part attributed to unresolved processes and the biases in salinity (Section 3.1.1): a positive salinity bias leads to weaker vertical stratification and thus an overall deeper mixed layer (Figure A3). While the broad spatial patterns of MLD during the summer agree with those in CARIB12 and other datasets, the patterns during the winter do not appear to be as well represented in the CESM-POP simulations and further highlight the important role of Amazon river runoff and salinity in the Caribbean Sea (Figure A3d and A3e). The biases in the CESM-POP simulated MLD are larger than those compared to CARIB12 and GLORYS12, highlighting the importance of processes across scales to properly resolve regional mixed layer depths, but also the sensitivity of the definition of MLD and vertical grids in the models (Treguier et al., 2023).

3.3   Vertical structure and water mass properties

We compare the vertical structure of the water column in CARIB12, with GLORYS12 and with available observations along WOCE lines A20 and A22 within the region of interest (Figure 1b). Figure 8 shows joint probability functions of Temperature-Salinity for CARIB12, GLORYS12 and GO-SHIP CTD data (Figure 8a-8c, respectively; CARIB12 and GLORYS12 data are co-located in space and time with profiles along the WOCE lines): the overall vertical structure and water mass characteristics is well represented in CARIB12, with some of the largest differences occurring in the Caribbean surface waters (Figure 8d-8e). These differences are not surprising, surface waters exhibit higher variability as they are exposed to a number of large scale circulation and forcing mechanisms, e.g. the influence of river runoff at sub-seasonal to seasonal scales, wind-driven circulation, eddies and the Caribbean Current (Corredor and Morell, 2001; Jouanno et al., 2012; Digna et al., 2018; Seijo-Ellis et al., 2023). Additional biases are noted around the salinity maximum (Subtropical Underwaters, as described in e.g. Seijo-Ellis et al., 2019; Torres et al., 2023) where there is a wider spread in values in CARIB12 compared to GLORYS12 and GO-SHIP. Nevertheless, the biases in the sub-surface salinity maximum are small and the model shows good agreement with GLORYS12 and observations. These differences may reflect larger variability in the sub-surface inflow associated with the North Atlantic gyre and/or the formation of the SUW mass in the North Atlantic.

A comparison between CARIB12 and GLORYS12 for the area-weighted time mean profile of salinity and temperature in the region of interest (Figure 9) shows a salty and slight cold bias near the surface (consistent with the discussion in Section 3.1). At depth, the biases are reversed with a fresh bias in the $100 - 150$ m depth range, which corresponds to the sub-surface salinity maximum associated with Subtropical Underwaters, and a warm bias of up to $0.5°C$. Biases in the mean profiles of temperature and salinity get smaller with depth (Figure 9). Biases seen in Figure 9 are representative of the biases in Figures 10 and 13, which show that CARIB12 reproduces well the large scale signals in both temperature and salinity across the length of the simulation.

The area weighted seasonal cycle of salinity and temperature in CARIB12 is in good agreement with GLORYS12 (Figure 10). Model biases indicate the amplitude of the seasonal cycle in CARIB12 is well represented compared to GLORYS12. The near-surface biases in the seasonal cycle of temperature and salinity are of the same order as those shown in Section 3.1. Figure 10a-10c shows the strong seasonal cycle in salinity for the region that is largely driven by the runoff from the Amazon and Orinoco rivers during late boreal spring through early fall and the higher salinity during late fall through winter into early spring driven by the lower riverine input to the ocean and the inflow of saltier Atlantic waters. These results highlight CARIB12's ability to correctly represent temperature and salinity variability in the CS and surrounding regions at seasonal scales.

Figure 11 shows the seasonal anomalies in salinity (a-c) and temperature (d-f) for the sub-region east of the minor Antilles (see sub-regions in Figure A5). CARIB12 reproduces well the signals of temperature and salinity of the waters outside the eastern CS. The largest salinity biases ($\approx 25\%$) occur near the surface during the summer months which agree well with the biases shown in Figure 3. These biases are reduced at depth. The temperature biases in this sub-region remain below ($\approx 10\%$). Within the eastern Caribbean Sea (region CS.E in Figure A5), the salinity biases are reduced below $\approx 25\%$ and the temperature biases remain below $\approx 10\%$. This indicates that salinity biases resulting from the limitations in the specification of the freshwater runoff are drastically reduced as the waters enter the CS, the main region of interest in the development of CARIB12.

At inter-annual timescales, CARIB12 salinity and temperature anomalies in the upper 300 m are overall consistent with GLORYS12 (Figure 13). The largest anomalies in GLORYS12 are also present in CARIB12, including signals likely associated with the 2015/2016 La Niña (salty and warm anomalies from 2015 onwards, Jiménez-Muñoz et al., 2016) and the biases associated with those signals are generally below $\approx 20\%$. It is worth noting that the signals associated with these anomalies are not only captured in the horizontal mean of temperature and salinity, but their vertical signature is also well represented in CARIB12. Within the CS (Figure 14), interannual anomalies are also well captured in CARIB12 although differences in the magnitude and amplitude of some of the signals leads to larger biases when compared to the full validation region shown in Figure 13. For example, the salty and warm signal between 2016 and 2020 has a longer duration in CARIB12 but the magnitude of the anomalies is not as large as in GLORYS12. The attenuation of these interannual anomalies may also be related to the specification of the horizontal viscosity parameters in the model and added effect of tides in CARIB12 driving enhanced vertical mixing not represented in GLORYS12. Further evaluation of these effects is worth additional examination but remain beyond the scope of this work.

3.4 Transports

Proper representation of ocean mass transports into the CS is important to ensure the processes and properties within it are also well represented. Ocean mass transports were calculated for passages in the eastern and northern Caribbean Sea. The passages are shown in Figure 1b and a summary of the mean transports in CARIB12, GLORYS12 and observational estimates can be found in Table 4 (for each of the passages of interest). We note that while transports based on CARIB12 and GLORYS12 are a time mean during 2000-2020, observational estimates are available only for shorter periods of time (often outside the 2000-2020 period of the simulation).

The mean transport across the Windward Passage between Cuba and Hispaniola is 1.91 Sv into the Caribbean Sea which is lower than that in GLORYS12 (2.8 Sv) and observational based estimates (3.8/3.6 Sv) by Smith et al. (2007). Nevertheless, Johns et al. (2002) and Smith et al. (2007) indicate there is still uncertainties on the transport through this passage.

The inflow across the Mona Passage (0.38 Sv) is also underestimated in CARIB12 compared to observations (3.0 Sv); here, GLORYS12 has a net outflow of 1.22 Sv which, along with the freshwater shown for GLORYS in Figure 3b (red contour in the region of the Domincan Republic and Puerto Rico), may be a significant contributor to the biases seen in the region when comparing CARIB12 to GLORYS12 (e.g. Figure 3c).

Flow through the Anegada Passage is an important contributor to the circulation between the Atlantic and the Caribbean Sea: CARIB12 shows good agreement with observations by Johns et al. (2002) with a 1.53 Sv inflow compared to 2.5 Sv. However, recent studies suggest that the inflow through the Anegada Passage may be larger than previously thought (e.g., Gradone et al., 2023). CARIB12 captures the mean transport through the Anegada Passage better than GLORYS12 which has a mean outflow of 0.14 Sv.

The Antigua Passage mean inflow is 2.11 Sv in CARIB12 which compares favorably against 3.1 Sv estimated by Johns et al. (2002) and is about half the transport in GLORYS12 (-4.06 Sv). Across the Guadeloupe Passage the inflow in CARIB12 (0.74 Sv) agrees better with observations (1.1 Sv) than GLORYS12 (0.10 Sv). Similarly for the Dominica Passage, although both CARIB12 (2.79 Sv) and GLORYS12 (3.02 Sv) overestimate the inflow here compared to 1.6 Sv inflow estimated by Johns et al. (2002). The St. Lucia Passage mean inflow in CARIB12 agrees well with observations (1.97 Sv in CARIB12 and 1.5 Sv from observations) while GLORYS12 overestimates the inflow by 3.4 Sv.

The St. Lucia - Trinidad section (Figure 1b) is a combination of the St. Vincent and Grenada Passages in Johns et al. (2002). CARIB12 has a mean inflow of 9.51 Sv which agrees well with the 8.6 Sv estimate by Johns et al. (2002). Along this section, GLORYS12 has a mean inflow almost twice as large (16.62 Sv) as that suggested by observations, which may also contribute to near-surface biases in the CS (particularly the southern part) discussed in Sections 3.1 and 3.1.2.

The net mean inflow to the Caribbean Sea is 20.94 Sv which is 0.31 Sv more than the mean flow out of the Caribbean Sea via the Yucatan Channel (20.63 Sv) (Figure 1). The mean flow through the Yucatan Channel in CARIB12 is ≈ 3 Sv less than that estimated from observations by Sheinbaum et al. (2002) and Candela et al. (2003) (23.8 and 23.06 Sv, respectively); it is also ≈ 7 Sv below GLORYS12 and the most recent estimate of 27.6 Sv by Candela et al. (2019). The difference in mean transport across observational estimates collected in different years may indicate low frequency variability that is not well-captured in

CARIB12 and is partially captured in GLORYS12. Also, the estimates by Sheinbaum et al. (2002) and Candela et al. (2019) are based on observations between September 1999 and June 2001, whereas the estimate in Candela et al. (2019) is based on observations between September 2012 and August 2016. We also note that the section defining the Yucatan Channel in CARIB12 is not completely bounded by land which may result in a lower mean outflow there.

At sub-seasonal timescales, CARIB12 shows less variability compared to GLORYS12 (Figure 15), which is reminiscent of the negative biases in surface speed and EKE described in Section 3.1.2. At seasonal timescales, there is an overall agreement between CARIB12 and GLORYS12 (Figure 16a-16f). With the exception of the Guadeloupe and Dominica Passages (Figure 16c and 16d), GLORYS12 shows stronger seasonal variability than CARIB12. We note that, as the seasonal cycle is regulated by the seasonal freshwater runoff from the Amazon and Orinoco river plumes (Wilson and Johns, 1997; Corredor and Morell, 2001; Johns et al., 2002; Chérubin and Richardson, 2007; Jouanno et al., 2012; Seijo-Ellis et al., 2023), differences in how the runoff is represented in the two models (runoff is applied in the subsurface in GLORYS12 vs at the surface in CARIB12) may have implications for the across-passage transports and thus result in differences between CARIB12 and GLORYS12. Finally, GLORYS12 shows stronger inter-annual variability than CARIB12 (Figure 16g-16l). While the mean inter-annual flows are well represented in CARIB12, the model does not capture the same amplitude of variability that GLORYS12 suggests exists in some the passages (Figures 16g-l). These differences may be further indicators of the differences between the models: runoff specification, horizontal viscosity configuration and the overall differences in model forcing (i.e. GloFAS runoff in CARIB12 versus runoff climatology in GLORYS12). Continuous observations would be needed to better assess how CARIB12 represents variability across timescales in the transports across the numerous passages. Nevertheless, both CARIB12 and GLORYS12 indicate that the flow across these passages is complex and highly variable which has been highlighted by previous studies and remains an active area of research (Wilson and Johns, 1997; Johns et al., 1999; Centurioni and Niiler, 2003; Johns et al., 2002; Gradone et al., 2023).

4 Conclusions

A new regional ocean-only CESM/MOM6 configuration of the Caribbean Sean is validated for the present day (2000-2020) against the GLORYS12 reanalysis and a suite of observation-based datasets. Near-surface fields of temperature, salinity and SSH are well represented, with small mean biases, comparable standard deviations and high correlations between CARIB12, GLORYS12 and the respective observation based datasets for each field. In particular, the seasonal cycle of SSS and the spatial pattern of the low salinity associated with the Amazon river plume is well captured. Eddy Kinetic energy shows some negative biases within the Caribbean Sea, yet the seasonal variability is captured. The MLD is also well represented, with a deep winter mixed layer and a shallow summer MLD, and biases against the GLORYS12 reanalysis generally less than 3m. While not shown, a simple comparison of SSHa time series with tidal gauges was completed and shows general good agreement with stations across the Caribbean Sea and Gulf of Mexico. The mean flows are also well represented across the domain with good agreement when comparing to GLORYS12. Further tuning of the horizontal viscosity and choice of parameters may be needed to improve the biases in near-surface fields, particularly mesoscale variability across the Caribbean Sea.

The vertical structure of the water column is well captured in CARIB12 compared to GLORYS12 and GO-SHIP data. The largest differences are observed in the near-surface water mass and in the layer of the sub-surface salinity maximum which, in CARIB12, is broader and not as pronounced as in the GLORYS12 reanalysis and GO-SHIP data. Nevertheless, the overall vertical structure is reproduced accurately in CARIB12. Vertical temperature and salinity variability is also overall well represented across timescales. While some differences exist at sub-seasonal timescales, the seasonal cycle is represented well. Across the full simulation, anomalies in temperature and salinity across the water column are comparable to those in the reanalysis.

Ocean mass transports across a number of passages in the northern and eastern Caribbean sea are computed and compared against GLORYS12 and observations. The mean flows in CARIB12 compare favorably against observations while GLORYS12 exhibits some biases, particularly along the Mona Passage, Anegada Passage and the St.Lucia - Trinidad section. The seasonal and inter-annual transports in CARIB12 compare overall well with GLORYS12, yet GLORYS12 exhibits larger variability in some cases. GLORYS12 suggests larger variability at sub-seasonal timescales too. Nevertheless, there are no observations available long enough to assess the variability of the flows along the passages across different timescales.

We compared mean fields for SST, SSS and MLD of CARIB12 against a $1°$ resolution CESM-POP configuration. While the CESM-POP captures the mean state and broad patterns of SST in the CS, it does not represent well significant dynamical features that drive variability in the region. For example, the location, spatial extent and magnitude of both the Caribbean Current and the upwelling system in South America are not well represented. In addition, there are biases in SSS and the representation of the Amazon and Orinoco river plumes. The extent and seasonal amplitude of the SSS cycle is not well captured including unresolved mesoscale and sub-mesoscale instabilities that drive much of the variability within the CS. These salinity biases may also be responsible for large biases seen in the mixed layer depth suggesting that the low resolution does not represent the regional vertical stratification and variability to a good degree. CARIB12 improves these biases significantly, highlighting the need of high-resolution regional models in order to properly address climate impacts at these scales and support decision making.

The main biases in CARIB12 can be attributed to two sources. The first, limitations in the specification of the freshwater runoff. The second, the need of further fine-tuning of the horizontal viscosity configuration and the need for higher-order parameterizations for high-resolution configurations like this one. CARIB12 is a test bed for the development of new schemes and parameterizations that can address these sources of biases and enhance the regional capabilities of CESM-MOM6.

With this thorough validation we showcase the new capabilities within CESM to perform high resolution regional ocean modeling. CARIB12 and the new regional ocean capabilities of CESM are invaluable tools for regional climate impact studies. As a community model configuration available to the wider scientific community, CARIB12 is a valuable tool for actionable science at regional scales and provides the foundations for further development of regional ocean climate modeling and downscaling within CESM. For example, as part of a separate project, the CARIB12 configuration will be used for dynamical downscaling of CESM climate projections to examine changes in the heat and salinity budgets of the Caribbean Sea under future climates.

Code and data availability. CARIB12 was developed on CESM and model components version $cesm2\_3\_alpha16b$. This and other versions of CESM are published and available via NSF-NCAR at www.cesm.ucar.edu:/models/cesm2/). A copy of the specific version used for CARIB12 is also hosted here: https://doi.org/10.5281/zenodo.11289425. CARIB12 configuration and input files can be accessed here: https://doi.org/10.5281/zenodo.11165669. CARIB12 output fields presented in this manuscript can be accessed here: https://doi.org/10.5281/zenodo.11264010. Trajectories generated with Ocean Parcels v2.0 and CARIB12 surface velocities, as well as the Ocean Parcels code used to generate the trajectories can be found here: https://doi.org/10.5281/zenodo.11267616. The datasets used for model forcing and validation are listed as follows: GLORYS12 reanalysis (https://doi.org/10.48670/moi00021, Global Ocean Physics Reanalysis, 2021); OISST v2 (https://psl.noaa.gov/data/gridded/data.noaa.oisst.v2.highres.html, Huang et al. 2021); mixed layer depth (https://doi:10.1029/2004JC002378, de-Boyer Montégut, 2004); global total ekman and surface currents (https://doi.org/10.48670/mds-00327, Rio et al. 2014); TPXO9 (https://www.tpxo.net/home, Egbert and Erofeeva, 2002); Multi Observation Global Ocean Sea Surface Salinity (https://doi.org/10.48670/moi-00052, Droghei et al. 2016); CCHDO Hydrographic Data (CCHDO Hydrographic Data Office, 2023.)

Author contributions. Conceptualization: G.S-E., D.G., G.M., F.B., Model configuration: G.S-E., D.G., G.M., F.B., Model simulations: G.S-E, G.M., Model Evaluation: G.S-E., D.G., G.M., F.B., Formal Analysis: G.S-E., D.G., G.M., Visualization: G.S-E., D.G., G.M., Original Draft: G.S-E., Review and Editing: G.S-E., D.G., G.M., F.B.

Competing interests. The authors declare no competing interests.

Acknowledgements. G.S-E. and D.G. acknowledge support by NSF award 2026954 and NOAA award NA21OAR4310261. Part of the work by G.S-E. was completed under the NSF NCAR ASP-Graduate Visitors Program. This material is based upon work supported by the National Center for Atmospheric Research, which is a major facility sponsored by the National Science Foundation under Cooperative Agreement No. 1852977. We would like to acknowledge high-performance computing support from Cheyenne (doi:10.5065/D6RX99HX) provided by NSF NCAR's Computational and Information Systems Laboratory, sponsored by the National Science Foundation. We would also like to acknowledge valuable input provided by the informal MOM6 Regional Modeling meetings led by Dr. Charles Stock (NOAA/GFDL) and Dr. Andrew Ross (NOAA/GFDL). We recognize valuable input and support from the Earth System Modeling Group at Rutgers University, in particular Dr. Enrique Curchitser, Dr. James Simkins, Dr. Nicole Laureanti, Mr. Rob Cermak, and Mr. Raphael Dussain (Rutgers/GFDL). In addition, we would like to acknowledge valuable assistance and input from Dr. Michael Levy and other members of the Ocean Section at NSF NCAR. The authors would also like to thank two anonymous reviewers for their comments and suggestions towards improving this manuscript.

References

Accad, Y. and Pekeris, C. L.: Solution of the tidal equations for the M2 and S2 tides in the world oceans from a knowledge of the tidal potential alone, Philosophical Transactions of the Royal Society of London. Series A, Mathematical and Physical Sciences, 290, 235–266, 1978.

Adcroft, A. and Campin, J.-M.: Rescaled height coordinates for accurate representation of free-surface flows in ocean circulation models, Ocean Modelling, 7, 269–284, 2004.

Adcroft, A., Anderson, W., Balaji, V., Blanton, C., Bushuk, M., Dufour, C. O., Dunne, J. P., Griffies, S. M., Hallberg, R., Harrison, M. J., Held, I. M., Jansen, M. F., John, J. G., Krasting, J. P., Langenhorst, A. R., Legg, S., Liang, Z., McHugh, C., Radhakrishnan, A., Reichl, B. G., Rosati, T., Samuels, B. L., Shao, A., Stouffer, R., Winton, M., Wittenberg, A. T., Xiang, B., Zadeh, N., and Zhang, R.: The GFDL Global Ocean and Sea Ice Model OM4.0: Model Description and Simulation Features, Journal of Advances in Modeling Earth Systems, 11, 3167–3211, https://doi.org/https://doi.org/10.1029/2019MS001726, 2019.

Andrade, C. A. and Barton, E. D.: Eddy development and motion in the Caribbean Sea, Journal of Geophysical Research: Oceans, 105, 26 191–26 201, 2000.

Andrade-Amaya, C. A.: The circulation and variability of the Colombian Basin in the Caribbean Sea, Ph.D. thesis, Tesis Ph. D. University of Wales, Wales, 2000.

Arakawa, A. and Lamb, V. R.: Computational Design of the Basic Dynamical Processes of the UCLA General Circulation Model, in: General Circulation Models of the Atmosphere, edited by CHANG, J., vol. 17 of *Methods in Computational Physics: Advances in Research and Applications*, pp. 173–265, Elsevier, https://doi.org/https://doi.org/10.1016/B978-0-12-460817-7.50009-4, 1977.

Argo, G.: Argo float data and metadata from global data assembly centre (Argo GDAC), SEANOE, 2000.

Arias, P. A., Martínez, J. A., and Vieira, S. C.: Moisture sources to the 2010 - 2012 anomalous wet season in northern South America, Climate Dynamics, 45, 2861–2884, 2015.

Bowen, B. W., Rocha, L. A., Toonen, R. J., and Karl, S. A.: The origins of tropical marine biodiversity, Trends in ecology & evolution, 28, 359–366, 2013.

Brickman, D., Alexander, M. A., Pershing, A., Scott, J. D., and Wang, Z.: Projections of physical conditions in the Gulf of Maine in 2050, Elem Sci Anth, 9, 00 055, 2021.

Bryden, H. L., Longworth, H. R., and Cunningham, S. A.: Slowing of the Atlantic meridional overturning circulation at 25 N, Nature, 438, 655–657, 2005.

Cabanes, C., Grouazel, A., von Schuckmann, K., Hamon, M., Turpin, V., Coatanoan, C., Paris, F., Guinehut, S., Boone, C., Ferry, N., et al.: The CORA dataset: validation and diagnostics of in-situ ocean temperature and salinity measurements, Ocean Science, 9, 1–18, 2013.

Caesar, L., Rahmstorf, S., Robinson, A., Feulner, G., and Saba, V.: Observed fingerprint of a weakening Atlantic Ocean overturning circulation, Nature, 556, 191–196, 2018.

Candela, J., Tanahara, S., Crepon, M., Barnier, B., and Sheinbaum, J.: Yucatan Channel flow: Observations versus CLIPPER ATL6 and MERCATOR PAM models, Journal of Geophysical Research: Oceans, 108, 2003.

Candela, J., Ochoa, J., Sheinbaum, J., Lopez, M., Perez-Brunius, P., Tenreiro, M., Pallàs-Sanz, E., Athié, G., and Arriaza-Oliveros, L.: The flow through the Gulf of Mexico, Journal of Physical Oceanography, 49, 1381–1401, 2019.

CCHDO Hydrographic Data Office: CCHDO Hydrographic Data Archive, https://cchdo.ucsd.edu/, 2023.

Centurioni, L. R. and Niiler, P. P.: On the surface currents of the Caribbean Sea, Geophysical Research Letters, 30, 2003.

490

495

500

505

510

515

520

Chamberlain, M., Sun, C., Matear, R., Feng, M., and Phipps, S.: Downscaling the climate change for oceans around Australia, Geoscientific Model Development, 5, 1177–1194, 2012.

Chérubin, L. and Richardson, P. L.: Caribbean current variability and the influence of the Amazon and Orinoco freshwater plumes, Deep Sea Research Part I: Oceanographic Research Papers, 54, 1451–1473, 2007.

Chollett, I., Mumby, P. J., Müller-Karger, F. E., and Hu, C.: Physical environments of the Caribbean Sea, Limnology and Oceanography, 57, 1233–1244, 2012.

Coles, V. J., Brooks, M. T., Hopkins, J., Stukel, M. R., Yager, P. L., and Hood, R. R.: The pathways and properties of the Amazon River Plume in the tropical North Atlantic Ocean, Journal of Geophysical Research: Oceans, 118, 6894–6913, https://doi.org/https://doi.org/10.1002/2013JC008981, 2013.

Corredor, J. E. and Morell, J. M.: Seasonal variation of physical and biogeochemical features in eastern Caribbean Surface Water, Journal of Geophysical Research: Oceans, 106, 4517–4525, https://doi.org/https://doi.org/10.1029/2000JC000291, 2001.

Danabasoglu, G., Large, W. G., Tribbia, J. J., Gent, P. R., Briegleb, B. P., and McWilliams, J. C.: Diurnal coupling in the tropical oceans of CCSM3, Journal of climate, 19, 2347–2365, 2006.

Danabasoglu, G., Yeager, S. G., Bailey, D., Behrens, E., Bentsen, M., Bi, D., Biastoch, A., Böning, C., Bozec, A., Canuto, V. M., et al.: North Atlantic simulations in coordinated ocean-ice reference experiments phase II (CORE-II). Part I: mean states, Ocean Modelling, 73, 76–107, 2014.

Danabasoglu, G., Lamarque, J.-F., Bacmeister, J., Bailey, D. A., DuVivier, A. K., Edwards, J., Emmons, L. K., Fasullo, J., Garcia, R., Gettelman, A., Hannay, C., Holland, M. M., Large, W. G., Lauritzen, P. H., Lawrence, D. M., Lenaerts, J. T. M., Lindsay, K., Lipscomb, W. H., Mills, M. J., Neale, R., Oleson, K. W., Otto-Bliesner, B., Phillips, A. S., Sacks, W., Tilmes, S., van Kampenhout, L., Vertenstein, M., Bertini, A., Dennis, J., Deser, C., Fischer, C., Fox-Kemper, B., Kay, J. E., Kinnison, D., Kushner, P. J., Larson, V. E., Long, M. C., Mickelson, S., Moore, J. K., Nienhouse, E., Polvani, L., Rasch, P. J., and Strand, W. G.: The Community Earth System Model Version 2 (CESM2), Journal of Advances in Modeling Earth Systems, 12, e2019MS001 916, https://doi.org/https://doi.org/10.1029/2019MS001916, e2019MS001916 2019MS001916, 2020.

de Boyer Montégut, C., Madec, G., Fischer, A. S., Lazar, A., and Iudicone, D.: Mixed layer depth over the global ocean: An examination of profile data and a profile-based climatology, Journal of Geophysical Research: Oceans, 109, 2004.

Delandmeter, P. and Sebille, E. v.: The Parcels v2. 0 Lagrangian framework: new field interpolation schemes, Geoscientific Model Development, 12, 3571–3584, 2019.

Digna, T. R.-R., Tal, E., and Frank, E. M.-K.: Description and Mechanisms of the Mid-Year Upwelling in the Southern Caribbean Sea from Remote Sensing and Local Data, Journal of Marine Science and Engineering, 6, 36, https://doi.org/10.3390/jmse6020036, 2018.

Droghei, R., Nardelli, B. B., and Santoleri, R.: Combining in situ and satellite observations to retrieve salinity and density at the ocean surface, Journal of Atmospheric and Oceanic Technology, 33, 1211–1223, 2016.

Egbert, G. D. and Erofeeva, S. Y.: Efficient Inverse Modeling of Barotropic Ocean Tides, Journal of Atmospheric and Oceanic Technology, 19, 183 – 204, https://doi.org/https://doi.org/10.1175/1520-0426(2002)019<0183:EIMOBO>2.0.CO;2, 2002.

Ezer, T., Heyman, W. D., Houser, C., and Kjerfve, B.: Modeling and observations of high-frequency flow variability and internal waves at a Caribbean reef spawning aggregation site, Ocean Dynamics, 61, 581–598, 2011.

Flather, R. A.: A tidal model of the north-west European continental shelf, 1976.

560   Fox-Kemper, B., Danabasoglu, G., Ferrari, R., Griffies, S., Hallberg, R., Holland, M., Maltrud, M., Peacock, S., and Samuels, B.: Param-
       eterization of mixed layer eddies. III: Implementation and impact in global ocean climate simulations, Ocean Modelling, 39, 61–78,
       2011.

       Frajka-Williams, E., Ansorge, I. J., Baehr, J., Bryden, H. L., Chidichimo, M. P., Cunningham, S. A., Danabasoglu, G., Dong, S., Donohue,
       K. A., Elipot, S., et al.: Atlantic meridional overturning circulation: Observed transport and variability, Frontiers in Marine Science, p.

565   260, 2019.

       Giese, G. S., Chapman, D. C., Black, P. G., and Fornshell, J. A.: Causation of large-amplitude coastal seiches on the Caribbean coast of
       Puerto Rico, Journal of physical oceanography, 20, 1449–1458, 1990.

       Godfrey, J. and Lindstrom, E.: The heat budget of the equatorial western Pacific surface mixed layer, Journal of Geophysical Research:
       Oceans, 94, 8007–8017, 1989.

570   Gradone, J. C., Wilson, W. D., Glenn, S., and Miles, T. N.: Upper Ocean Transport in the Anegada Passage from Multi-Year Glider Surveys,
       Authorea Preprints, 2023.

       Griffies, S., Levy, M., Adcroft, A., Danabasoglu, G., Hallgberg, R.W., a. J. D. a. L. W., and Ringler, T.: Theory and Numerics of the
       Community Ocean Vertical Mixing (CVMix) Project, Tech. rep., 2015.

       Griffies, S. M. and Hallberg, R. W.: Biharmonic friction with a Smagorinsky-like viscosity for use in large-scale eddy-permitting ocean

575   models, Monthly Weather Review, 128, 2935–2946, https://doi.org/10.1175/1520-0493(2000)128<2935:BFWASL>2.0.CO;2, 2000.

       Grodsky, S. A., Johnson, B. K., Carton, J. A., and Bryan, F. O.: Interannual Caribbean salinity in satellite data and model simulations, Journal
       of Geophysical Research: Oceans, 120, 1375–1387, https://doi.org/https://doi.org/10.1002/2014JC010625, 2015.

       Hormann, V., Centurioni, L. R., and Reverdin, G.: Evaluation of drifter salinities in the subtropical North Atlantic, Journal of Atmospheric
       and Oceanic Technology, 32, 185–192, 2015.

580   Hourdin, F., Mauritsen, T., Gettelman, A., Golaz, J.-C., Balaji, V., Duan, Q., Folini, D., Ji, D., Klocke, D., Qian, Y., Rauser, F., Rio, C.,
       Tomassini, L., Watanabe, M., and Williamson, D.: The Art and Science of Climate Model Tuning, Bulletin of the American Meteorological
       Society, 98, 589 – 602, https://doi.org/https://doi.org/10.1175/BAMS-D-15-00135.1, 2017.

       Huang, B., Liu, C., Banzon, V., Freeman, E., Graham, G., Hankins, B., Smith, T., and Zhang, H.-M.: Improvements of the daily optimum
       interpolation sea surface temperature (DOISST) version 2.1, Journal of Climate, 34, 2923–2939, 2021.

585   Hurrell, J. W., Holland, M. M., Gent, P. R., Ghan, S., Kay, J. E., Kushner, P. J., Lamarque, J.-F., Large, W. G., Lawrence, D., Lindsay, K.,
       Lipscomb, W. H., Long, M. C., Mahowald, N., Marsh, D. R., Neale, R. B., Rasch, P., Vavrus, S., Vertenstein, M., Bader, D., Collins, W. D.,
       Hack, J. J., Kiehl, J., and Marshall, S.: The Community Earth System Model: A Framework for Collaborative Research, Bulletin of the
       American Meteorological Society, 94, 1339 – 1360, https://doi.org/https://doi.org/10.1175/BAMS-D-12-00121.1, 2013.

       Jackson, L., Hallberg, R., and Legg, S.: A parameterization of shear-driven turbulence for ocean climate models, Journal of Physical Oceanog-

590   raphy, 38, 1033–1053, 2008.

       Jean-Michel, L., Eric, G., Romain, B.-B., Gilles, G., Angélique, M., Marie, D., Clément, B., Mathieu, H., Olivier, L. G., Charly,
       R., et al.: The Copernicus global 1/12 oceanic and sea ice GLORYS12 reanalysis, Frontiers in Earth Science, 9, 698 876,
       https://doi.org/https://doi.org/10.3389/feart.2021.698876, 2021.

       Jiawei Zhuang, Dussin, R., Huard, D., Bourgault, P., Banihirwe, A., Stephane Raynaud, Brewster Malevich, Schupfner, M., , Filipe, Levang,

595   S., Gauthier, C., Jüling, A., Almansi, M., RichardScottOZ, RondeauG, Rasp, S., Smith, T. J., Stachelek, J., Plough, M., , Pierre, Bell, R.,
       Caneill, R., and Xianxiang Li: pangeo-data/xESMF: v0.8.2, https://doi.org/10.5281/ZENODO.4294774, 2023.

Jiménez-Muñoz, J. C., Mattar, C., Barichivich, J., Santamaría-Artigas, A., Takahashi, K., Malhi, Y., Sobrino, J. A., and Schrier, G. v. d.: Record-breaking warming and extreme drought in the Amazon rainforest during the course of El Niño 2015–2016, Scientific reports, 6, 33 130, 2016.

600   Johns, E., Wilson, W. D., and Molinari, R. L.: Direct observations of velocity and transport in the passages between the Intra-Americas Sea and the Atlantic Ocean, 1984–1996, Journal of Geophysical Research: Oceans, 104, 25 805–25 820, 1999.

Johns, W. E., Townsend, T. L., Fratantoni, D. M., and Wilson, W.: On the Atlantic inflow to the Caribbean Sea, Deep Sea Research Part I: Oceanographic Research Papers, 49, 211–243, https://doi.org/https://doi.org/10.1016/S0967-0637(01)00041-3, 2002.

Jouanno, J., Sheinbaum, J., Barnier, B., Molines, J. M., and Candela, J.: Seasonal and interannual modulation of the eddy kinetic energy in
605   the Caribbean Sea, Journal of Physical Oceanography, 42, 2041–2055, 2012.

Kay, J. E., Deser, C., Phillips, A., Mai, A., Hannay, C., Strand, G., Arblaster, J. M., Bates, S. C., Danabasoglu, G., Edwards, J., Holland, M., Kushner, P., Lamarque, J.-F., Lawrence, D., Lindsay, K., Middleton, A., Munoz, E., Neale, R., Oleson, K., Polvani, L., and Vertenstein, M.: The Community Earth System Model (CESM) Large Ensemble Project: A Community Resource for Studying Climate Change in the Presence of Internal Climate Variability, Bulletin of the American Meteorological Society, 96, 1333 – 1349,
610   https://doi.org/https://doi.org/10.1175/BAMS-D-13-00255.1, 2015.

Kirtman, B. P., Bitz, C., Bryan, F., Collins, W., Dennis, J., Hearn, N., Kinter, J. L., Loft, R., Rousset, C., Siqueira, L., et al.: Impact of ocean model resolution on CCSM climate simulations, Climate dynamics, 39, 1303–1328, 2012.

Kjerfve, B.: Tides of the Caribbean sea, Journal of Geophysical Research: Oceans, 86, 4243–4247, 1981.

Lange, M. and Sebille, E. v.: Parcels v0. 9: prototyping a Lagrangian ocean analysis framework for the petascale age, Geoscientific Model
615   Development, 10, 4175–4186, 2017.

Large, W. and Danabasoglu, G.: Attribution and impacts of upper-ocean biases in CCSM3, Journal of Climate, 19, 2325–2346, 2006.

Large, W. and Pond, S.: Open ocean momentum flux measurements in moderate to strong winds, Journal of physical oceanography, 11, 324–336, 1981.

Large, W. G., McWilliams, J. C., and Doney, S. C.: Oceanic vertical mixing: A review and a model with a nonlocal boundary layer parame-
620   terization, Reviews of geophysics, 32, 363–403, 1994.

Lukas, R. and Lindstrom, E.: The mixed layer of the western equatorial Pacific Ocean, Journal of Geophysical Research: Oceans, 96, 3343–3357, 1991.

Manizza, M., Le Quéré, C., Watson, A. J., and Buitenhuis, E. T.: Bio-optical feedbacks among phytoplankton, upper ocean physics and sea-ice in a global model, Geophysical Research Letters, 32, 2005.

625   Marchesiello, P., McWilliams, J. C., and Shchepetkin, A.: Open boundary conditions for long-term integration of regional oceanic models, Ocean modelling, 3, 1–20, 2001.

Meehl, G. A., Moss, R., Taylor, K. E., Eyring, V., Stouffer, R. J., Bony, S., and Stevens, B.: Climate Model Intercomparisons: Preparing for the Next Phase, Eos, Transactions American Geophysical Union, 95, 77–78, https://doi.org/https://doi.org/10.1002/2014EO090001, 2014.

Mercator Ocean: GLOBAL OCEAN GRIDDED L4 SEA SURFACE HEIGHTS AND DERIVED VARIABLES REPROCESSED (1993-
630   ONGOING), https://doi.org/10.48670/MOI-00148, 2021.

Miloslavich, P., Díaz, J. M., Klein, E., Alvarado, J. J., Díaz, C., Gobin, J., Escobar-Briones, E., Cruz-Motta, J. J., Weil, E., Cortes, J., et al.: Marine biodiversity in the Caribbean: regional estimates and distribution patterns, PloS one, 5, e11 916, 2010.

Morell, J. M., Corredor, J. E., and Merryfield, W. J.: Thermohaline staircases in a Caribbean eddy and mechanisms for staircase formation, Deep Sea Research Part II: Topical Studies in Oceanography, 53, 128–139, 2006.

635 Mukherjee, S., Wilson, D., Jobsis, P., and Habtes, S.: Numerical modeling of internal tides and submesoscale turbulence in the US Caribbean regional ocean, Scientific Reports, 13, 1091, 2023.

NASA Ocean Biology Processing Group: SEAWIFS-ORBVIEW-2 Level 3 Mapped Chlorophyll Data Version R2018.0, https://doi.org/10.5067/ORBVIEW-2/SEAWIFS/L3M/CHL/2018, 2018.

Orlanski, I.: A Simple Boundary Condition for Unbounded Hyperbolic Flows, Journal of Computational Physics, 21, 251–269, 1976.

640 Reichl, B. G. and Hallberg, R.: A simplified energetics based planetary boundary layer (ePBL) approach for ocean climate simulations., Ocean Modelling, 132, 112–129, 2018.

Restrepo, J. C., Ortíz, J. C., Pierini, J., Schrottke, K., Maza, M., Otero, L., and Aguirre, J.: Freshwater discharge into the Caribbean Sea from the rivers of Northwestern South America (Colombia): Magnitude, variability and recent changes, Journal of Hydrology, 509, 266–281, 2014.

645 Restrepo, J. C., Higgins, A., Escobar, J., Ospino, S., and Hoyos, N.: Contribution of low-frequency climatic–oceanic oscillations to streamflow variability in small, coastal rivers of the Sierra Nevada de Santa Marta (Colombia), Hydrology and Earth System Sciences, 23, 2379–2400, 2019.

Richards, K. J., Whitt, D. B., Brett, G., Bryan, F. O., Feloy, K., and Long, M. C.: The impact of climate change on ocean submesoscale activity, Journal of Geophysical Research: Oceans, 126, e2020JC016 750, 2021.

650 Rio, M.-H., Mulet, S., and Picot, N.: Beyond GOCE for the ocean circulation estimate: Synergetic use of altimetry, gravimetry, and in situ data provides new insight into geostrophic and Ekman currents, Geophysical Research Letters, 41, 8918–8925, 2014.

Roberts, M. J., Hewitt, H. T., Hyder, P., Ferreira, D., Josey, S. A., Mizielinski, M., and Shelly, A.: Impact of ocean resolution on coupled air-sea fluxes and large-scale climate, Geophysical Research Letters, 43, 10–430, 2016.

Ross, A. C., Stock, C. A., Adcroft, A., Curchitser, E., Hallberg, R., Harrison, M. J., Hedstrom, K., Zadeh, N., Alexander, M., Chen, W.,
655 Drenkard, E. J., du Pontavice, H., Dussin, R., Gomez, F., John, J. G., Kang, D., Lavoie, D., Resplandy, L., Roobaert, A., Saba, V., Shin, S.-I., Siedlecki, S., and Simkins, J.: A high-resolution physical-biogeochemical model for marine resource applications in the Northwest Atlantic (MOM6-COBALT-NWA12 v1.0), Geoscientific Model Development Discussions, 2023, 1–65, https://doi.org/10.5194/gmd-2023-99, 2023.

Rudzin, J., Shay, L. K., Jaimes, B., and Brewster, J.: Upper ocean observations in eastern Caribbean Sea reveal barrier layer within a warm
660 core eddy, Journal of Geophysical Research: Oceans, 122, 1057–1071, 2017.

Sadourny, R.: The dynamics of finite-difference models of the shallow-water equations, Journal of Atmospheric Sciences, 32, 680–689, 1975.

Schmidt, M. W., Spero, H. J., and Lea, D. W.: Links between salinity variation in the Caribbean and North Atlantic thermohaline circulation, Nature, 428, 160–163, 2004.

Seijo-Ellis, G., Lindo-Atichati, D., and Salmun, H.: Vertical Structure of the Water Column at the Virgin Islands Shelf Break and Trough,
665 Journal of Marine Science and Engineering, 7, 74, https://doi.org/10.3390/jmse7030074, 2019.

Seijo-Ellis, G., Giglio, D., and Salmun, H.: Intrusions of Amazon River Waters in the Virgin Islands Basin During 2007–2017, Journal of Geophysical Research: Oceans, 128, e2022JC018 709, 2023.

Sheinbaum, J., Candela, J., Badan, A., and Ochoa, J.: Flow structure and transport in the Yucatan Channel, Geophysical Research Letters, 29, 10–1, 2002.

670 Smith, R., Johns, W., and Johns, E.: Volume transport and variability at Windward Passage, in: AGU Spring Meeting Abstracts, vol. 2007, pp. OS52A–08, 2007.

Solano, M., Canals, M., and Leonardi, S.: Development and validation of a coastal ocean forecasting system for Puerto Rico and the US Virgin Islands, Journal of Ocean Engineering and Science, 3, 223–236, 2018.

Sosa, E. A.: Variabilidad Temporal de la Produccion Primaria Fitoplanctonica en la Estacion CATS: Con Enfasis en el Impacto de la Mare Interna Semidiurna sobre la Produccion, Ph.D. thesis, University of Puerto Rico - Mayaguez, 2001.

Southwick, O., Johnson, E., and McDonald, N.: A simple model for sheddies: Ocean eddies formed from shed vorticity, Journal of Physical Oceanography, 46, 2961–2979, 2016.

Tebaldi, C. and Knutti, R.: The use of the multi-model ensemble in probabilistic climate projections, Philosophical transactions of the royal society A: mathematical, physical and engineering sciences, 365, 2053–2075, 2007.

Torres, R. R., Latandret, S., Salon, J., and Dagua, C.: Water masses in the Caribbean Sea and sub-annual variability in the Guajira upwelling region, Ocean Dynamics, 73, 39–57, 2023.

Tozer, B., Sandwell, D. T., Smith, W. H., Olson, C., Beale, J., and Wessel, P.: Global bathymetry and topography at 15 arc sec: SRTM15+, Earth and Space Science, 6, 1847–1864, 2019.

Treguier, A. M., de Boyer Montégut, C., Bozec, A., Chassignet, E. P., Fox-Kemper, B., McC. Hogg, A., Iovino, D., Kiss, A. E., Le Sommer, J., Li, Y., Lin, P., Lique, C., Liu, H., Serazin, G., Sidorenko, D., Wang, Q., Xu, X., and Yeager, S.: The mixed-layer depth in the Ocean Model Intercomparison Project (OMIP): impact of resolving mesoscale eddies, Geoscientific Model Development, 16, 3849–3872, https://doi.org/10.5194/gmd-16-3849-2023, 2023.

Tsujino, H., Urakawa, S., Nakano, H., Small, R. J., Kim, W. M., Yeager, S. G., Danabasoglu, G., Suzuki, T., Bamber, J. L., Bentsen, M., et al.: JRA-55 based surface dataset for driving ocean–sea-ice models (JRA55-do), Ocean Modelling, 130, 79–139, 2018.

Tsujino, H., Urakawa, L. S., Griffies, S. M., Danabasoglu, G., Adcroft, A. J., Amaral, A. E., Arsouze, T., Bentsen, M., Bernardello, R., Böning, C. W., et al.: Evaluation of global ocean–sea-ice model simulations based on the experimental protocols of the Ocean Model Intercomparison Project phase 2 (OMIP-2), Geoscientific Model Development, 13, 3643–3708, 2020.

Tucker, T., Giglio, D., Scanderbeg, M., and Shen, S. S. P.: Argovis: A Web Application for Fast Delivery, Visualization, and Analysis of Argo Data, Journal of Atmospheric and Oceanic Technology, 37, 401 – 416, https://doi.org/10.1175/JTECH-D-19-0041.1, 2020.

Wilson, W. D. and Johns, W. E.: Velocity structure and transport in the Windward Islands Passages, Deep Sea Research Part I: Oceanographic Research Papers, 44, 487–520, 1997.

Zsoter, E., Harrigan, S., Barnard, C., Wetterhall, F., Ferrario, I., Mazzetti, C., Alfieri, L., Salamon, P., and Prudhomme, C.: River discharge and related historical data from the Global Flood Awareness System. v3.1., copernicus Climate Change Service (C3S) Climate Data Store (CDS). URL: https://cds.climate.copernicus.eu/cdsapp!/dataset/cems-glofas-historical (Accessed on 01-01-2023), 2021.

Table 1. Physical configuration, parameterization and parameter choices for CARIB12.

Parameter	Value	Reference
Time-stepping	Baroclinic 900 s	
	Thermodynamic 1800 s	
Grid		
Horizontal	$1/12°$	
Vertical	65 layer z*	
Open Boundary Conditions		
Barotropic	Flather	Flather (1976)
Baroclinic	Orlanski	Orlanski (1976)
	nudging timescales: 0.3 day for inflow	Marchesiello et al. (2001)
	and 360 days for outflow	
Tracers	Reservoir length scales:	
	3×10^4 m (out), 3,000 m (in)	
Tides		
Explicit from TPXO	10 tidal constituents:	Egbert and Erofeeva (2002)
	M2, S2, N2, K2, K1, O1,P1, Q1, MM, MF	
	tidal potential forcing as body force	
	in momentum equations across full domain	
Self-attraction and loading	coeff = 0.094	Accad and Pekeris (1978)
Background kinematic viscosity	$1.0 \times 10^{-6} \frac{m^2}{s}$	
Coriolis Discretization	SADOURNY75 Energy	Sadourny (1975)
Horizontal Mixing		
Horizontal viscosity	Laplacian	
Biharmonic horizontal viscosity	background: $5 \times 10^8 \frac{m^4}{s}$	
	Velocity ($\frac{m}{s}$) and Time (s) scales = 0	
Nonlinear eddy viscosity	Smagorinsky (constant = 0.02)	Griffies and Hallberg (2000)
Vertical Mixing	CvMix Library	Griffies et al. (2015)
Boundary layer	K-Profile Parameterization (KPP)	Large et al. (1994)
Background diapycnal diffusivity	$1.0 \times 10^{-6} \frac{m^2}{s}$	
Shear-driven turbulence	LMD94	Large et al. (1994)
Mixing due to double diffusion processes		Large et al. (1994),
		Danabasoglu et al. (2006)
Prandtl Number	1.0	
Nudging Layers	T, S, u and v from GLORYS monthly means	
	restoring time: 10 - 150 days	
Mixed Layer re-stratification	Front length scale = 1500 m	Fox-Kemper et al. (2011)
	Decay time scale = 2.59×10^6 s	

Table 2. Summary of datasets used in the validation of CARIB12 with their corresponding information. Datasets with a * next to their name are also used for the model forcing.

Dataset	Fields	Reference	Resolutions
GLORYS12v1 (GLORYS12)*	temperature, salinity, velocities, sea-surface height mixed layer depth	Jean-Michel et al. (2021)	Space: $\frac{1}{12}^\circ$ Time: daily, monthly Depth of first layer = 0.5 m
Optimally Interpolated SST v2 (OISST)	sea-surface temperatures	Huang et al. (2021)	Space: $\frac{1}{4}^\circ$ Time: monthly
Multi Observation Global Ocean Sea Surface Salinity (MOGO)	sea-surface salinity	Droghei et al. (2016)	Space: $\frac{1}{8}^\circ$ Time: monthly
Global Ocean Gridded L4 Sea Surface Heights (GOGSSH)	sea-surface height	Mercator Ocean (2021)	Space: $\frac{1}{4}^\circ$ Time: monthly
GLOBCURRENT	surface currents	Rio et al. (2014)	Space: $\frac{1}{4}^\circ$ Time: monthly
Deboyer MLD Climatology	mixed layer depth	de Boyer Montégut et al. (2004)	Space: $1^\circ \times 1^\circ$ Time: monthly
CESM-POP	sea-surface temperature, sea-surface salinity, mixed layer depth	Tsujino et al. (2020)	Space: 1° Time: monthly Depth of first layer = 10 m

Table 3. Summary of mean and standard deviation of SST, SSS and MLD for CARIB12, GLORYS12 observational products and CESM-POP. Note that the CESM-POP simulation ends in 2018.

field	time range	model/dataset	mean	standard deviation
SST	2000-2020	CARIB12	27.50°C	0.53°C
		GLORYS12	27.63°C	0.56°C
		OISST	27.63°C	0.55°C
	2000-2018	CESM-POP	27.47°C	0.52°C
SSS	2000-2020 (DJF)	CARIB12	35.86 PSU	0.94 PSU
		GLORYS12	35.72 PSU	0.91 PSU
		MOGO	35.82 PSU	0.45 PSU
	2000-2018 (DJF)	CESM-POP	36.42 PSU	0.54 PSU
SSS	2000-2020 (JJA)	CARIB12	35.35 PSU	1.69 PSU
		GLORYS12	35.19 PSU	1.77 PSU
		MOGO	35.49 PSU	0.96 PSU
	2000-2018 (JJA)	CESM-POP	36.25 PSU	0.76 PSU
MLD	2000-2020 (DJF)	CARIB12	37.90 m	12.56 m
		GLORYS12	35.42 m	11.11 m
		Deboyer	41.80 m	10.52 m
	2000-2018 (DJF)	CESM-POP	66.22 m	17.46 m
MLD	2000-2020 (JJA)	CARIB12	17.49 m	7.21 m
		GLORYS12	17.55 m	4.72 m
		Deboyer	23.33 m	8.31 m
	2000-2018 (JJA)	CESM-POP	30.45 m	8.82 m

Table 4. Mean ocean transports (Sv) across passages in the Caribbean Sea: estimates from CARIB12 and the GLORYS12 reanalysis are for the period 2000-2020; estimates from observations are for the date ranges indicated in the table and are included together with relevant references. The location of each passage is shown in Figure 1. Negative transports correspond to a westward or southward flow, and positive transports to eastward or northward flows.

Passage	CARIB12	GLORYS	Observations [date range]	Observations reference
Windward Passage	-1.91	-2.8	-3.8/-3.6 [Oct '03–Feb '05]	Smith et al. (2007)
Mona Passage	-0.38	+1.22	-3.0 [Mar '96, Jul '96]	Johns et al. (2002)
Anegada Passage	-1.53	+0.14	-2.5 ± 1.4 [spread across the 1990's]	Johns et al. (2002)
			-4.8± 0.32 [Oct '20, Jul '21, Sep '21, Mar '22]	Gradone et al. (2023)
Antigua Passage	-2.11	-4.06	-3.1 ± 1.5 [spread across the 1990's]	Johns et al. (2002)
Guadeloupe Passage	-0.74	-0.10	-1.1 ± 1.1 [spread across the 1990's]	Johns et al. (2002)
Dominica Passage	-2.79	-3.02	-1.6 ± 1.2 [spread across the 1990's]	Johns et al. (2002)
St. Lucia Passage	-1.97	-4.92	-1.5 ± 2.4 [spread across the 1990's]	Johns et al. (2002)
St. Lucia - Trinidad	-9.51	-16.62	-8.6 [spread across the 1990's]	Johns et al. (2002)
Yucatan Passage	+20.63	+27.08	23.8 [Sept '99 - Jun '00]	Sheinbaum et al. (2002)
			+23.06 [Aug '99 - Jun '01]	Candela et al. (2003)
			+27.6 [Sept '12 - Aug '16]	Candela et al. (2019)
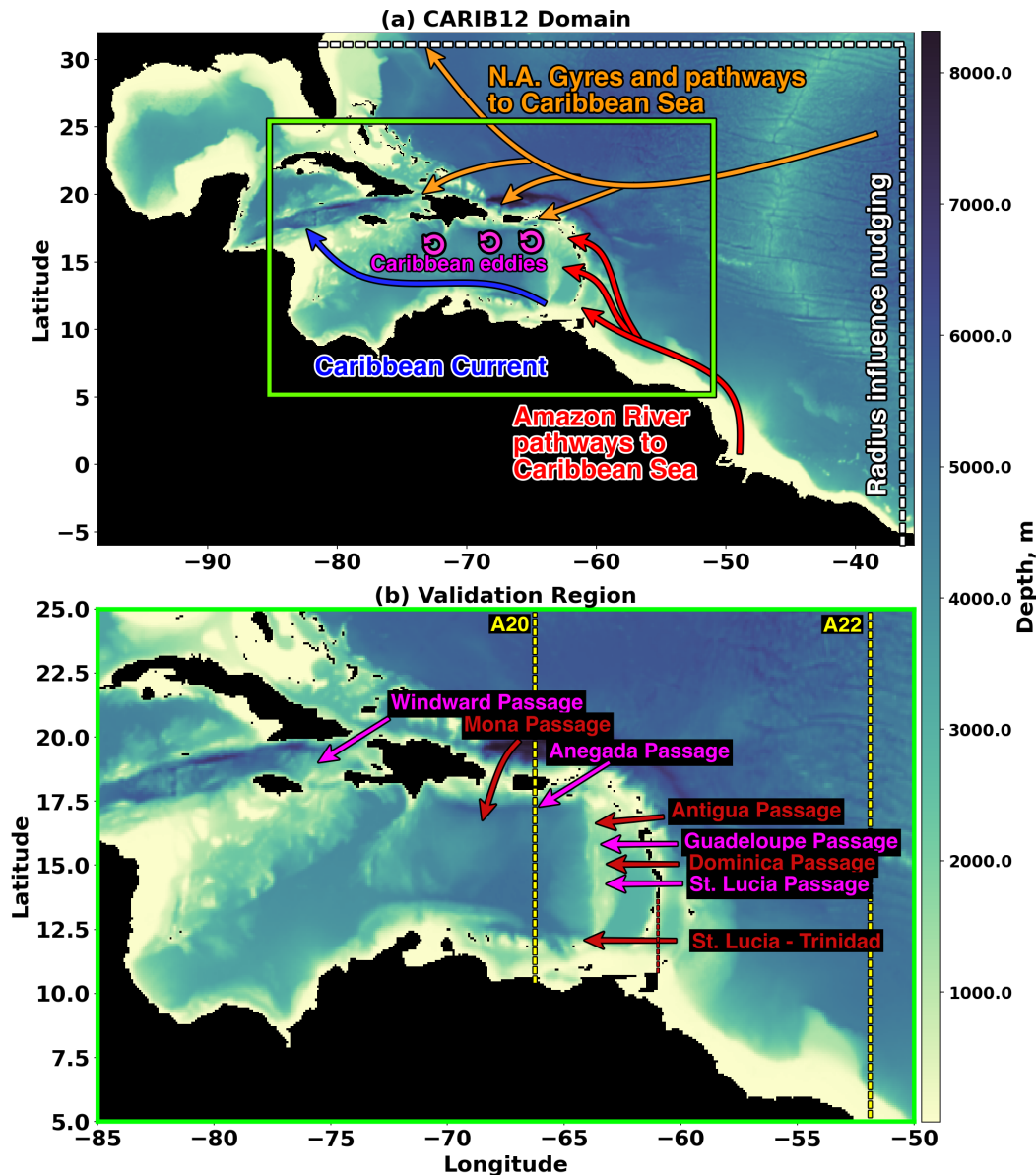
Figure 1. Model domain and topography. (a) CARIB12 regional domain and dominant processes regulating water properties in the Caribbean Sea. The northwestward flow of the Amazon river plume towards the Caribbean Sea is known to branch off in the three main pathways shown (red arrows). The plume waters can affect the vertical structure and strength of the Caribbean current (blue arrow). Interactions of the flow with the topography along the numerous passages at the Atlantic/Caribbean Sea interface generate mesoscale eddies (magenta) that entrain and transport waters westward. The North Atlantic Gyre dominates the near-surface inflow between the greater Antilles (orange). The deep flows there form an important return branch of the AMOC. White dashed lines show the radius of influence of boundary nudging layers in the configuration. The green box outlines the focus region for the analysis. (b) Validation and analysis region. Arrows indicate mean flow direction across the multiple passages in the eastern Caribbean Sea and between Greater Antilles. Yellow dashed lines show approximate location of WOCE lines A20 and A22 used in the validation.
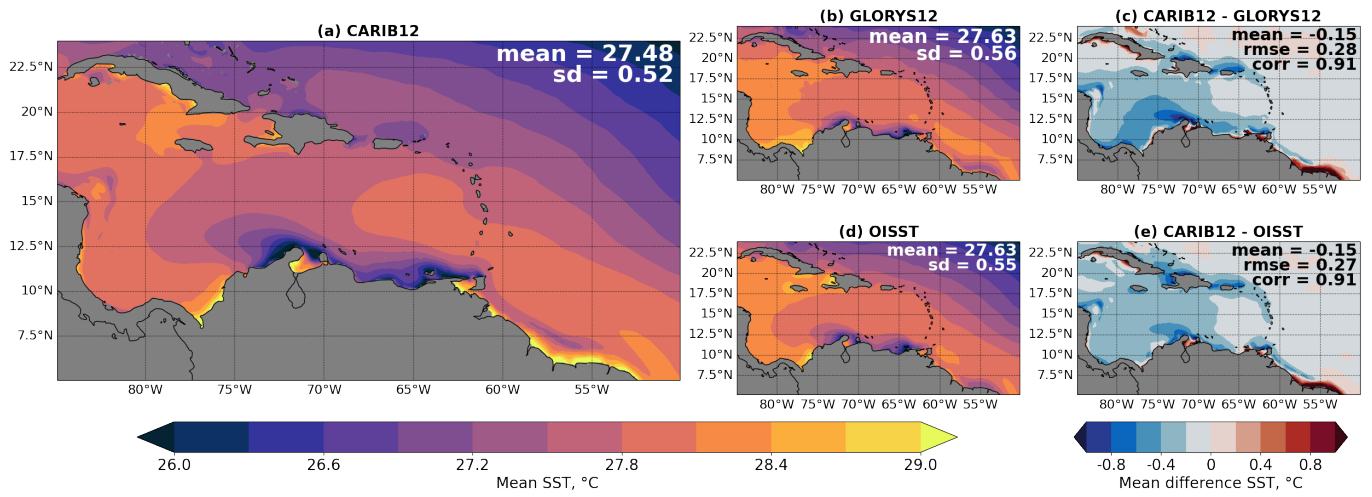
Figure 2. Time mean SST (°C) in the region of interest for this study (green box in Figure 1), during 2000-2020: (a) CARIB12, (b) GLORYS12, (c) CARIB12 minus GLORYS12, (d) OISST, (e) CARIB12 minus OISST. Mean and standard deviation are shown for each product (a, b and d). The mean bias, root mean squared error (rmse), and spatial correlation (corr) are shown in each comparison panel (c and e).
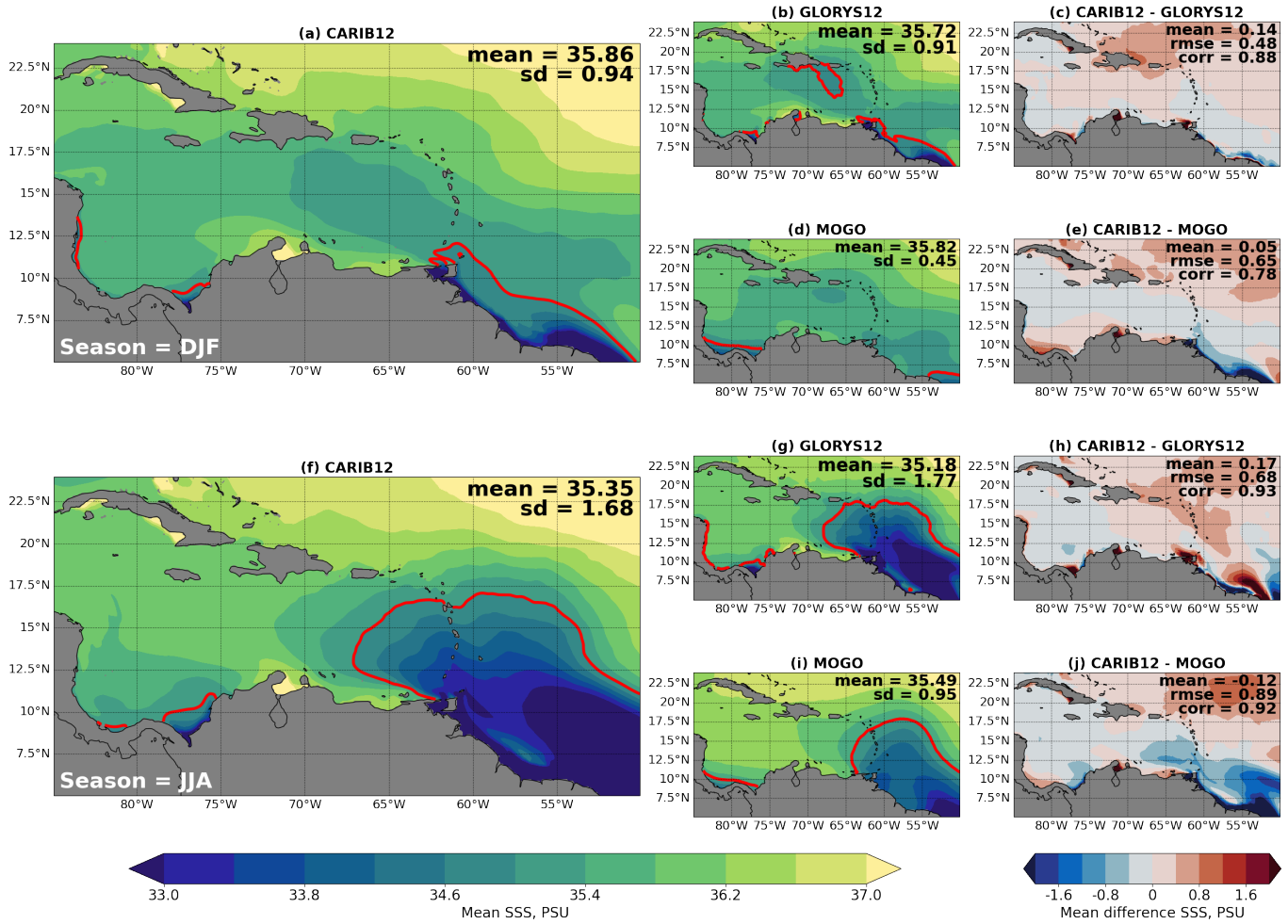
Figure 3. Time mean winter (a-e) and summer (f-j) SSS (PSU) in the region of interest for this study (green box in Figure 1): (a,f) CARIB12, (b,g) GLORYS12, (c,h) CARIB12 minus GLORYS12, (d,i) MOGO, (e,j) CARIB12 minus MOGO for winter and summer, respectively. The red line in panels (a, b, d, f, g, i) shows the 35 PSU isohaline as a proxy for the extent of the freshwater plumes from the Amazon and Orinoco rivers. Mean and standard deviation are shown for each product and seasonal mean. The mean bias, root mean squared error (rmse), and spatial correlation (corr) are shown in each comparison panel.
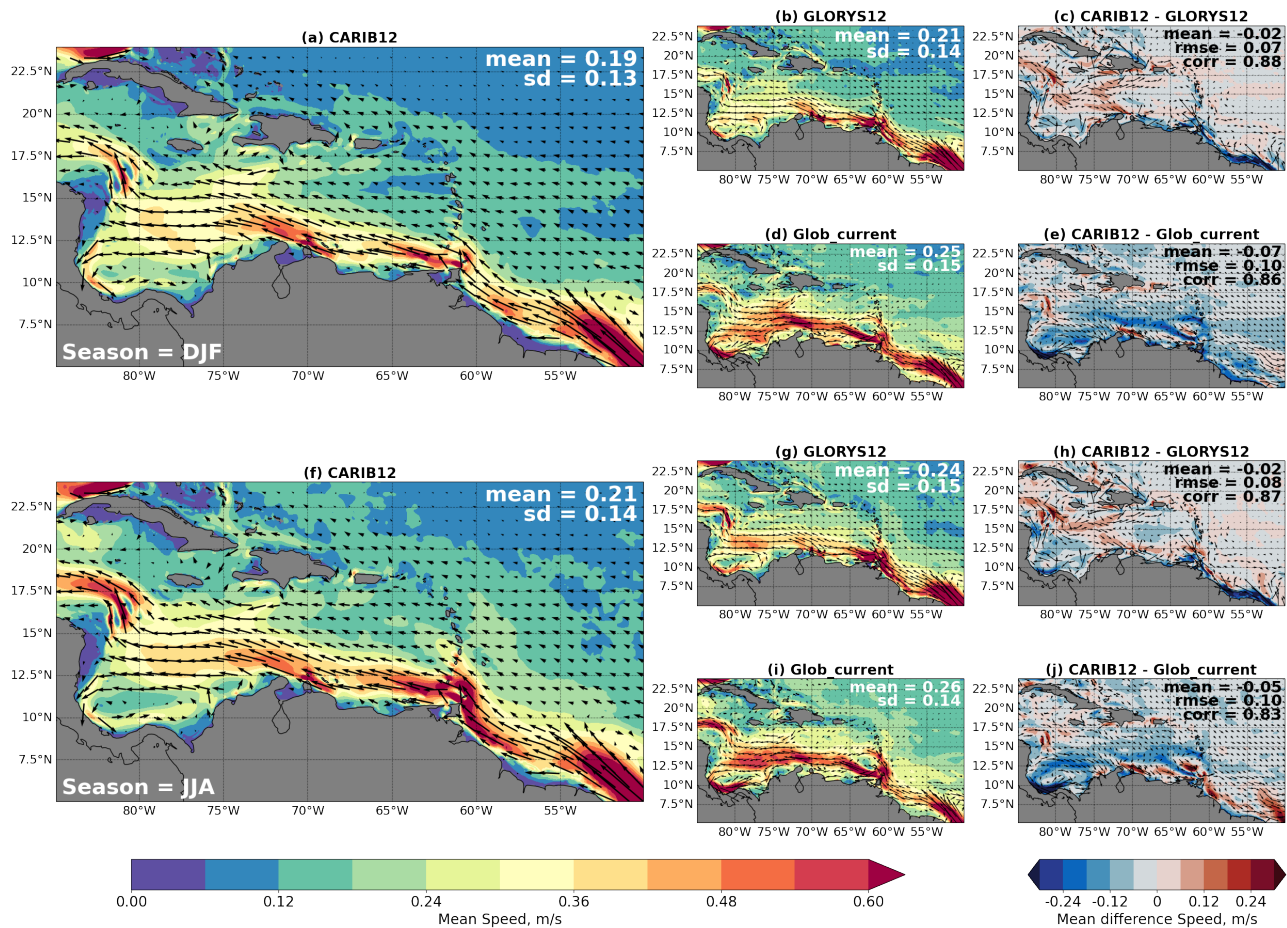
Figure 4. Time mean winter (a-e) and summer (f-j) surface speed (m/s) in the region of interest for this study (green box in Figure 1): (a,f) CARIB12, (b,g) GLORYS12, (c,h) CARIB12 minus GLORYS12, (d,i) GLOBCURRENT, (e,j) CARIB12 minus GLOBCURRENT for winter and summer, respectively. Black arrows show the direction of the surface flow with the size of the arrows scaled by the magnitude of the speed. Mean and standard deviation are shown for each product and seasonal mean. The mean bias, root mean squared error (rmse), and spatial correlation (corr) are shown in each comparison panel.
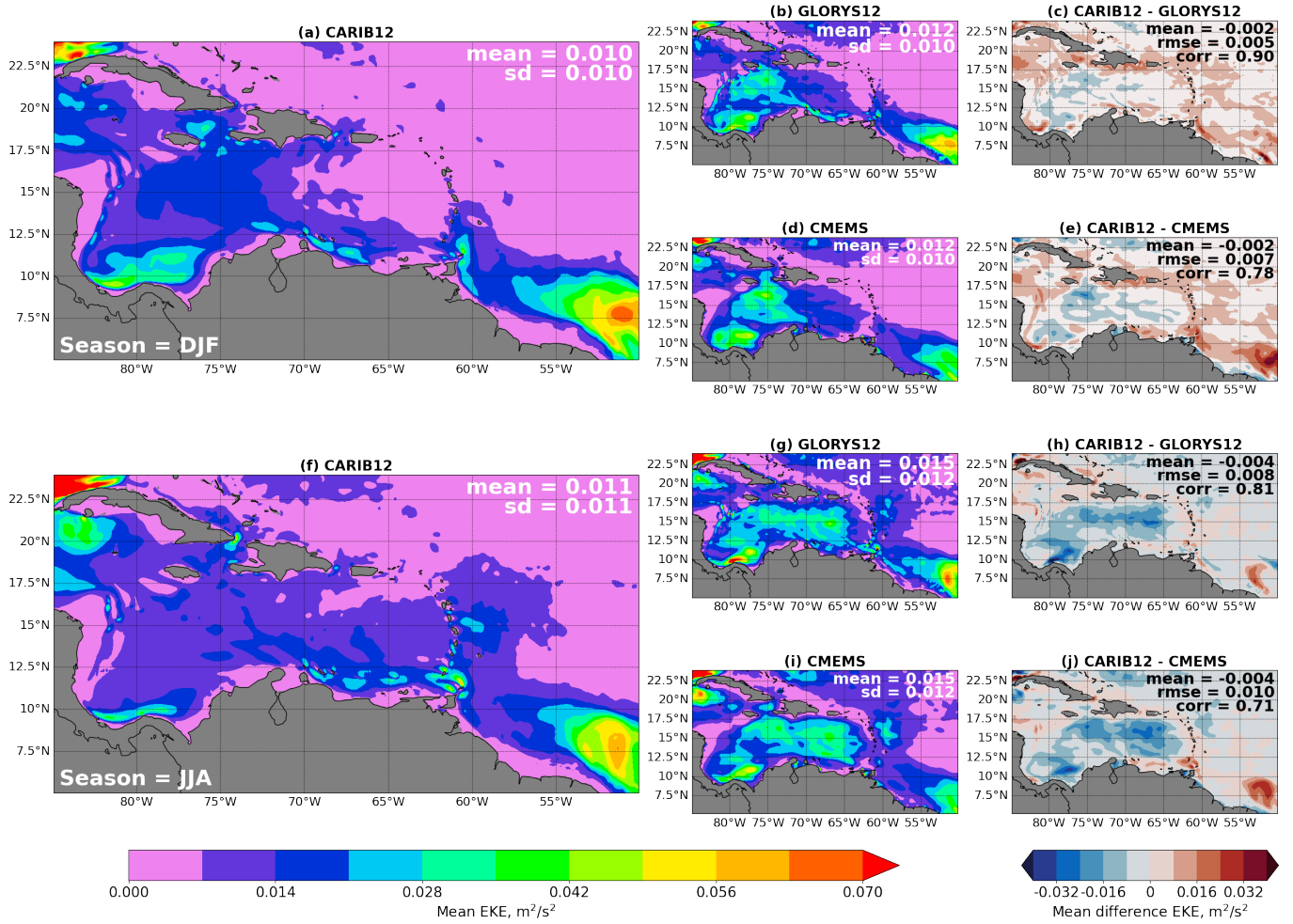
Figure 5. Time mean winter (a-e) and summer (f-j) EKE ($\frac{m^2}{s^2}$) in the region of interest for this study (green box in Figure 1): (a,f) CARIB12, (b,g) GLORYS12, (c,h) CARIB12 minus GLORYS12, (d,i) MOGO, (e,j) CARIB12 minus MOGO for winter and summer, respectively. The red line in panels (a, b, d, f, g, i) shows the 35 PSU isohaline as a proxy for the extent of the freshwater plumes from the Amazon and Orinoco rivers. Mean and standard deviation are shown for each product and seasonal mean. The mean bias, root mean squared error (rmse), and spatial correlation (corr) are shown in each comparison panel.
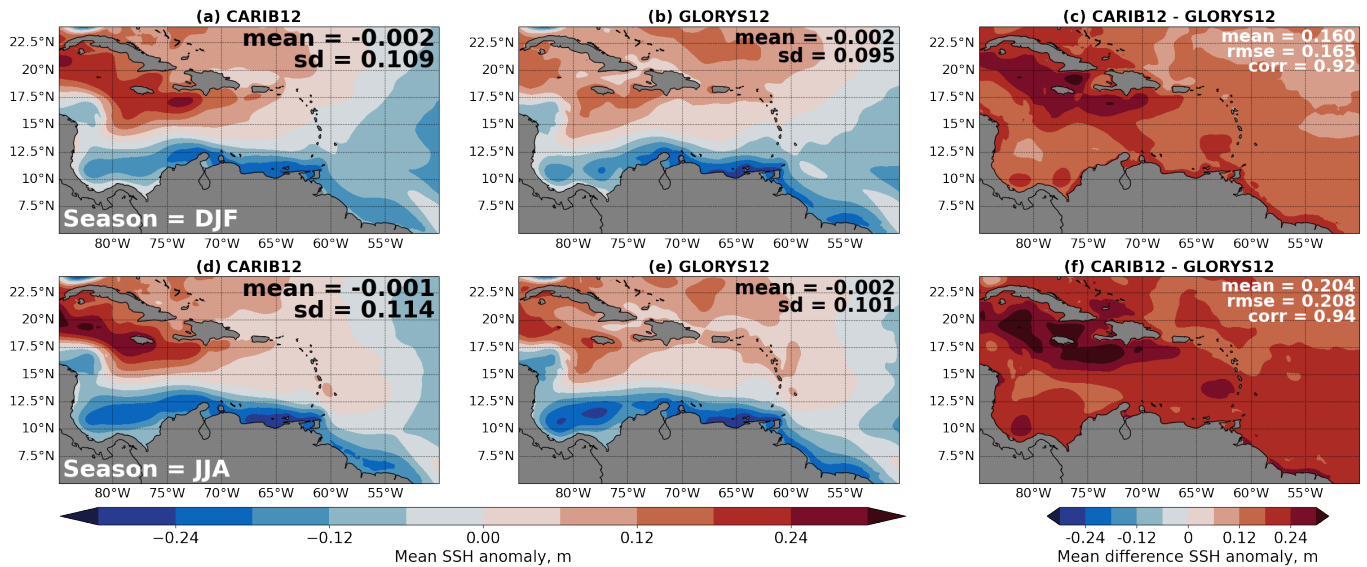
Figure 6. Time mean winter (a-c) and summer (d-f) SSH anomaly (SSHa, m) in the region of interest for this study (green box in Figure 1): (a,d) CARIB12, (b,e) GLORYS12, (c,f) CARIB12 minus GLORYS12 for winter and summer, respectively. The SSHa is the time mean SSH minus the spatial mean. Mean and standard deviation are shown for each product and seasonal mean. The mean bias, root mean squared error (rmse), and spatial correlation (corr) are shown in each comparison panel.
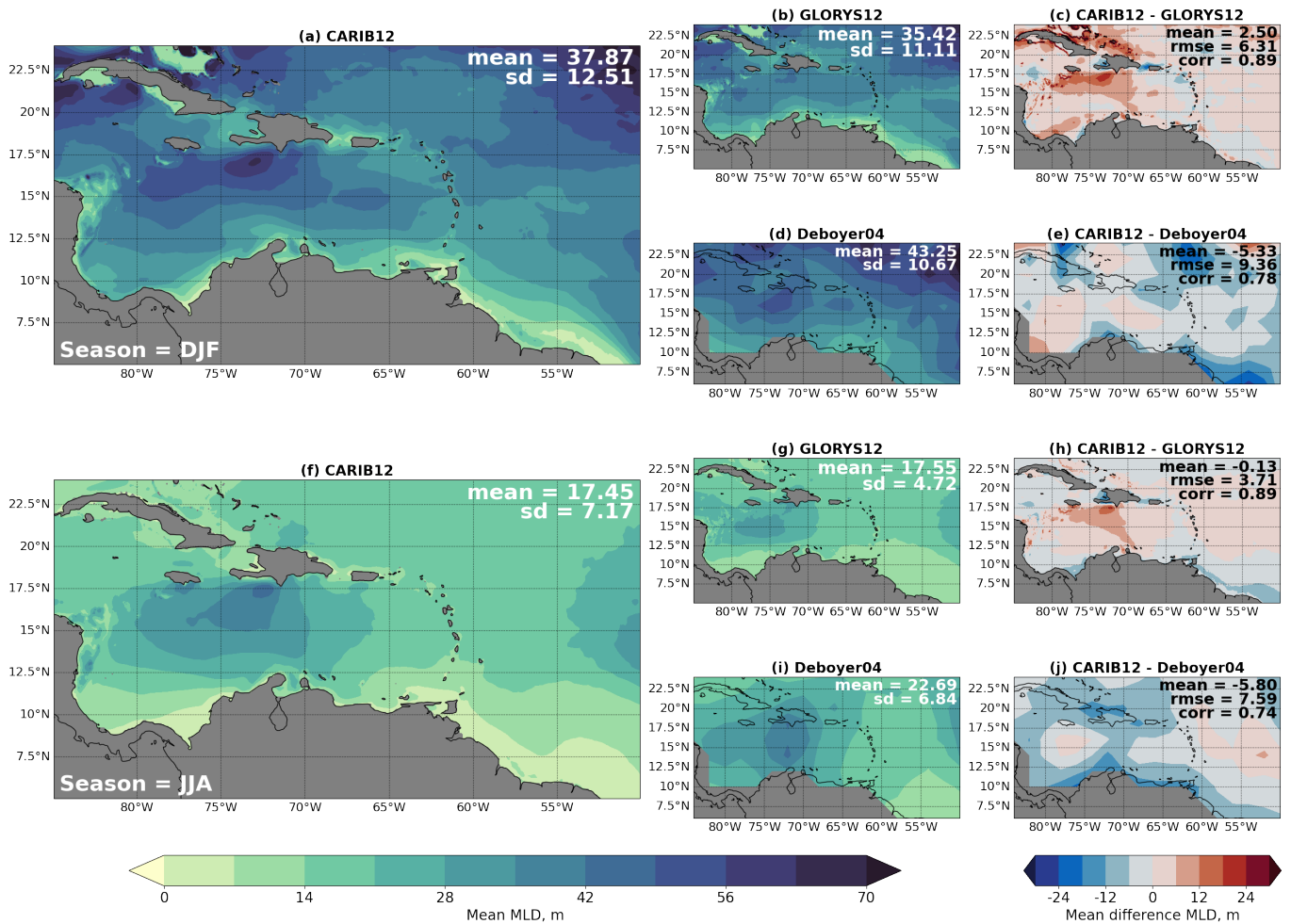
Figure 7. Time mean winter (a-e) and summer (f-j) MLD (m) in the region of interest for this study (green box in Figure 1): (a,f) CARIB12, (b,g) GLORYS12, (c,h) CARIB12 minus GLORYS12, (d,i) Deboyer, (e,j) CARIB12 minus Deboyer for winter and summer, respectively. Mean and standard deviation are shown for each product and seasonal mean. The mean bias, root mean squared error (rmse), and spatial correlation (corr) are shown in each comparison panel.
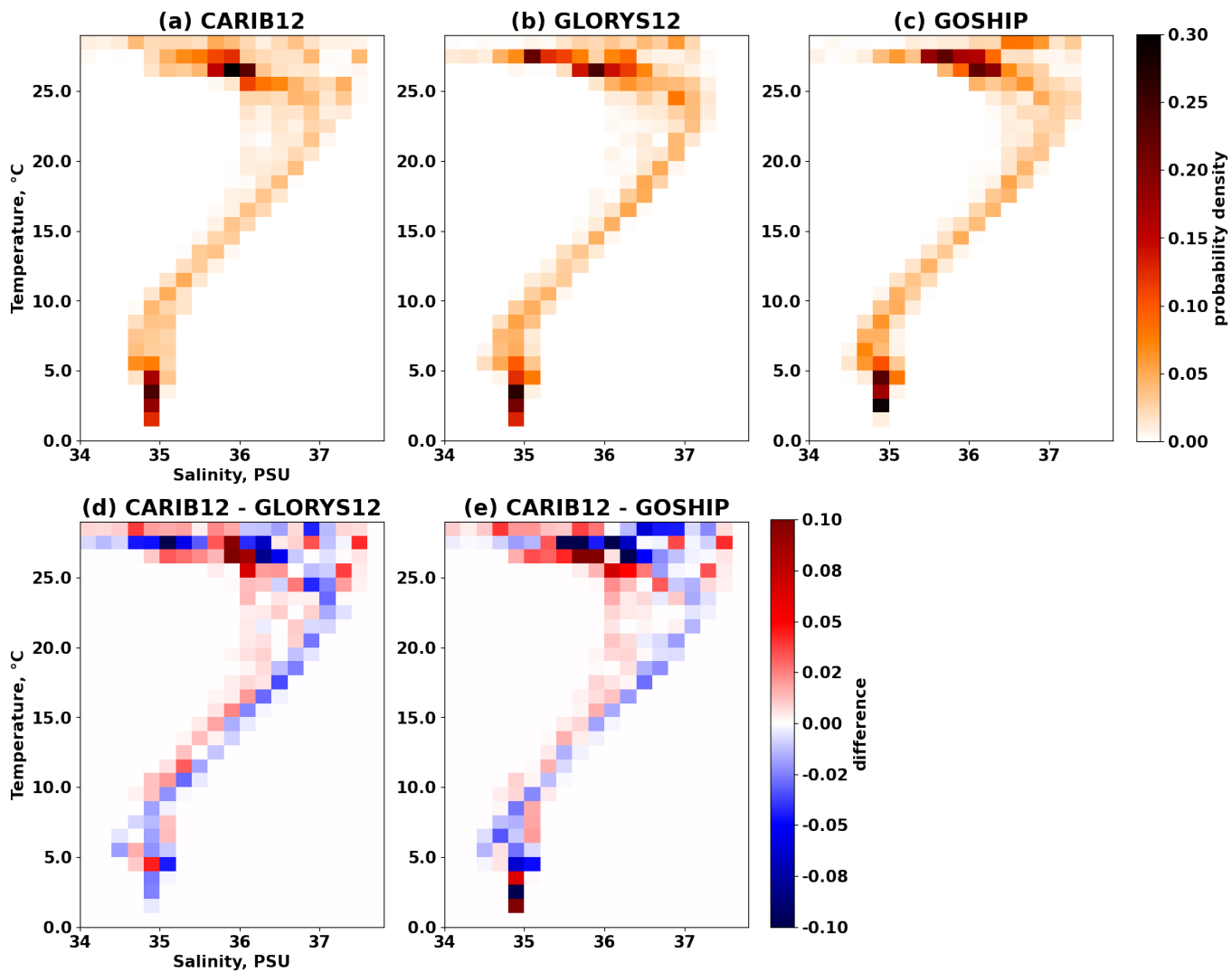
Figure 8. Temperature-Salinity joint probability density function for (a) CARIB12, (b) GLORYS12 and, (c) GO-SHIP. Panel (d) shows the difference between panel (a) and (b). Panel (e), the difference between (a) and (c).
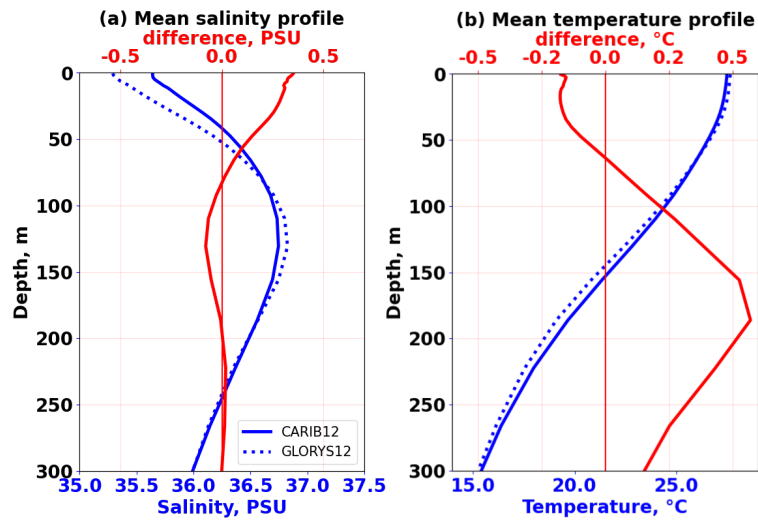
Figure 9. Time mean salinity (a) and temperature (b) profiles for the area average within the region of interest for this study (green box in Figure 1): CARIB12 (solid blue line) and GLORYS12 (dotted blue line). The difference between the two products is shown in red.
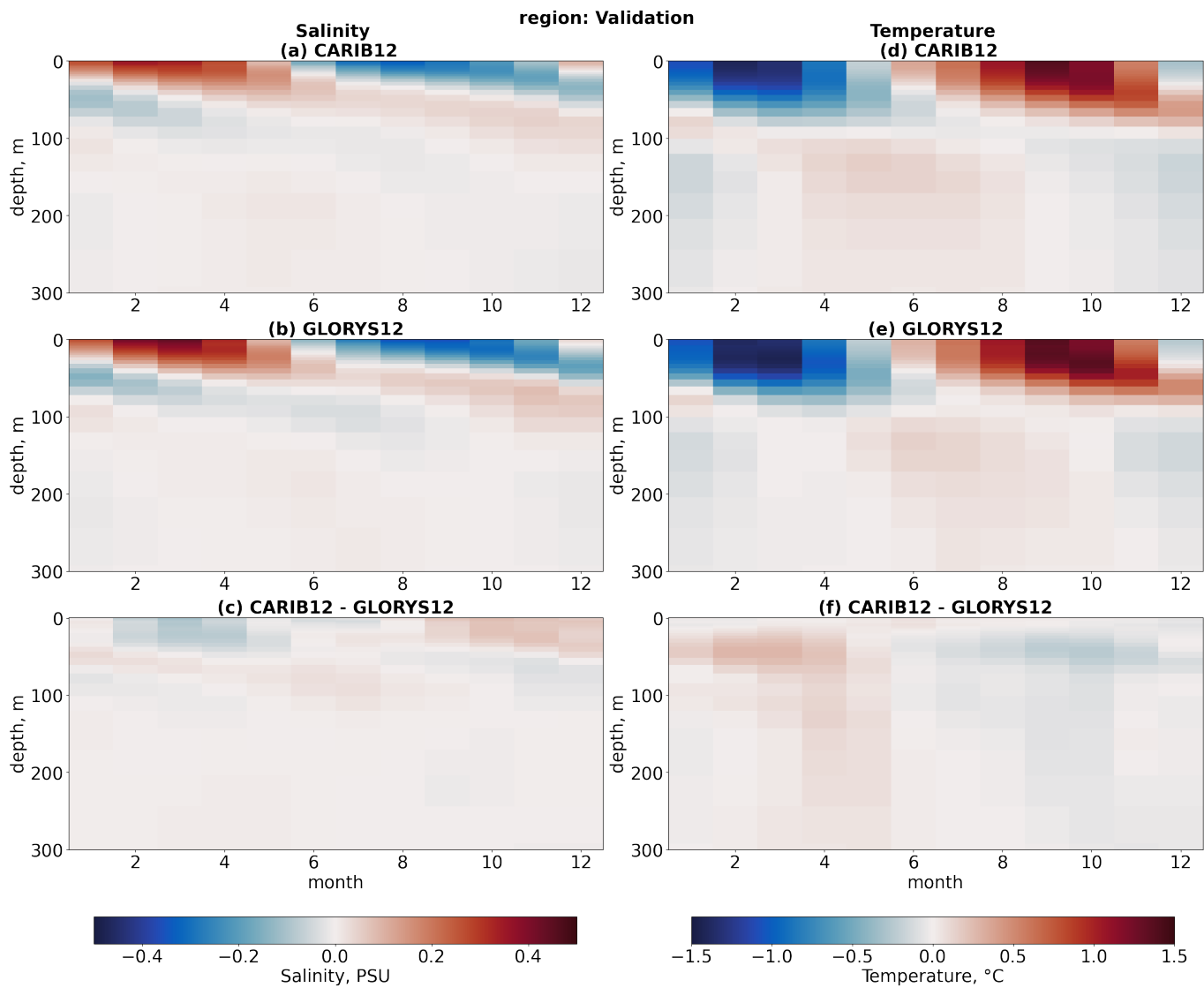
Figure 10. Area weighted mean seasonal salinity anomalies within the validation region (green box in Figure 1): (a) CARIB12, (b) GLO-RYS12, (c) difference between the products. Area weighted mean seasonal temperature anomaly within the validation region: (d) CARIB12, (e) GLORYS12, (f) difference between the products.
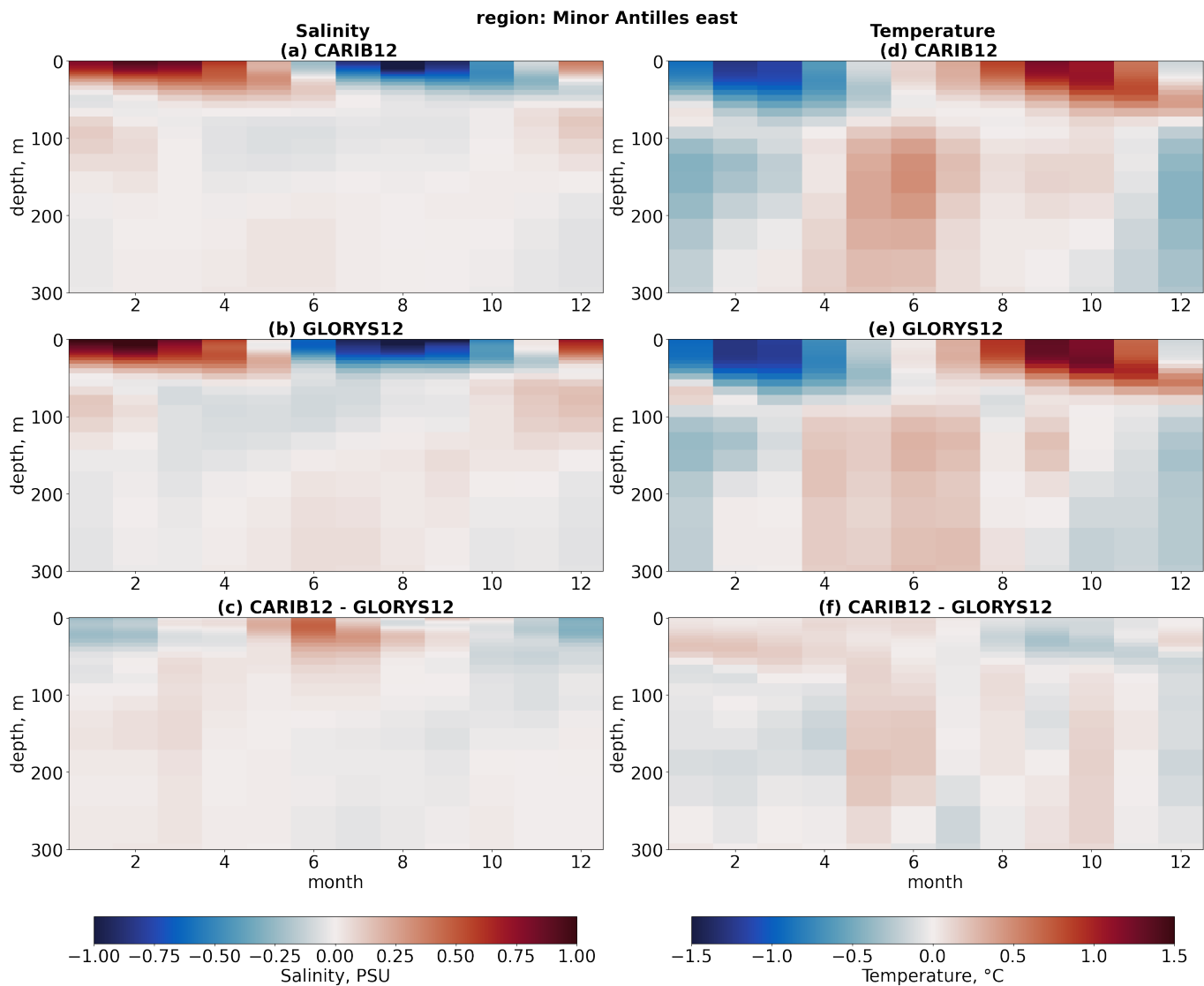
Figure 11. Area weighted mean seasonal salinity anomalies within the Minor Antilles east sub-region shown in Figure A5: (a) CARIB12, (b) GLORYS12, (c) difference between the products. Area weighted mean seasonal temperature anomaly within the validation region: (d) CARIB12, (e) GLORYS12, (f) difference between the products.
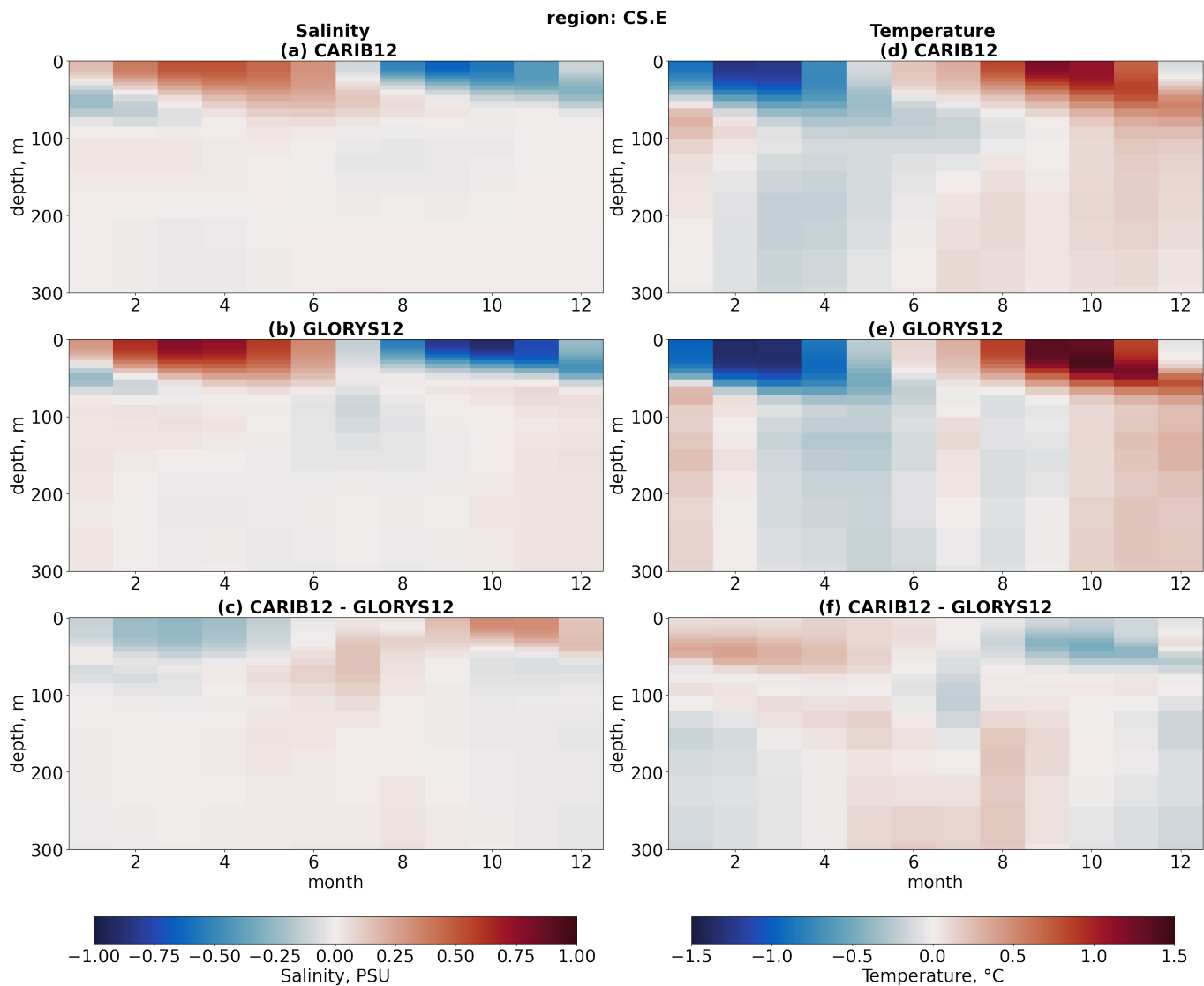
Figure 12. Area weighted mean seasonal salinity anomalies within the eastern CS region (CS.E) in Figure A5: (a) CARIB12, (b) GLORYS12, (c) difference between the products. Area weighted mean seasonal temperature anomaly within the validation region: (d) CARIB12, (e) GLORYS12, (f) difference between the products.
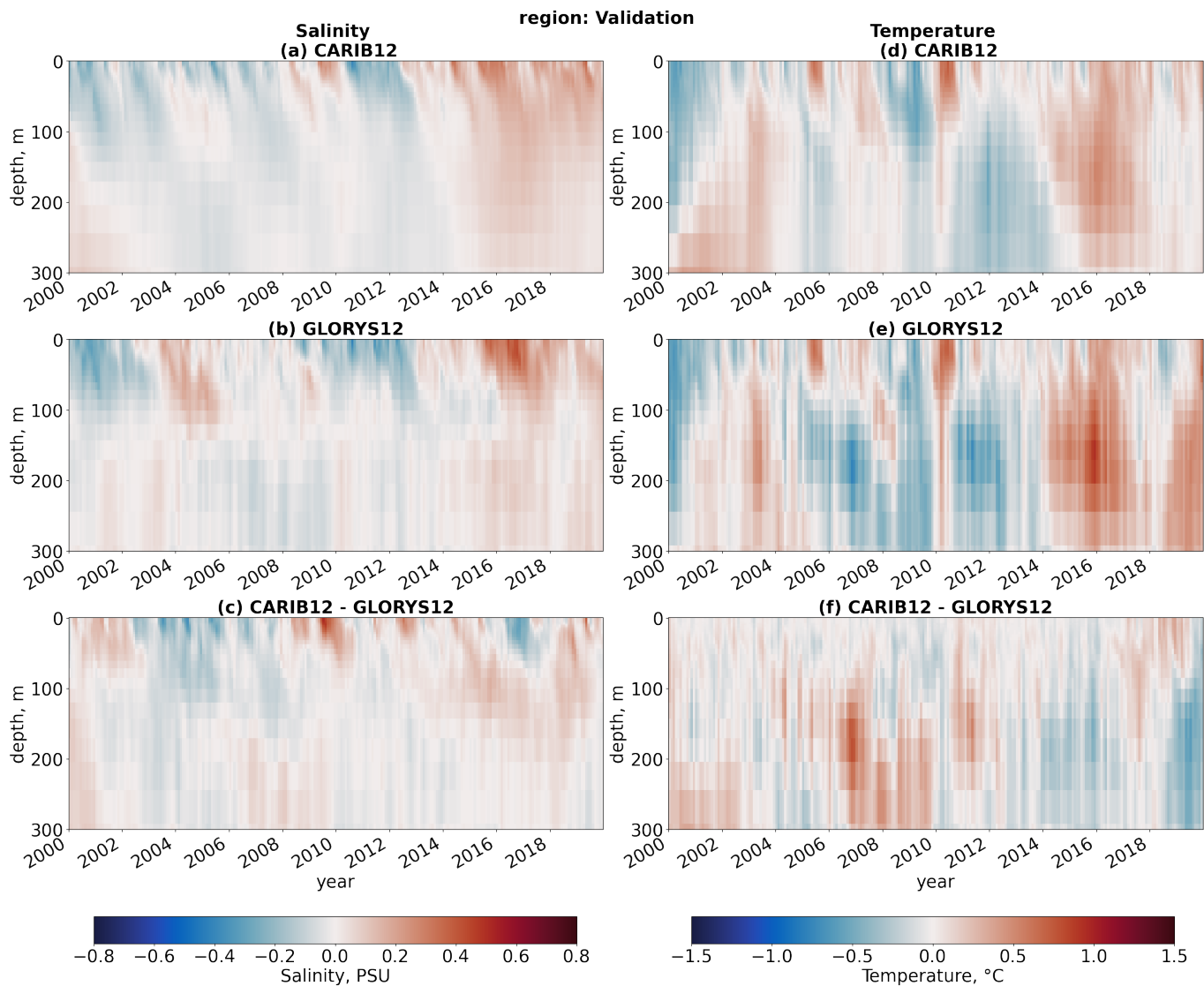
Figure 13. Area weighted mean monthly salinity anomaly within the validation region (green box in Figure 1): (a) CARIB12, (b) GLO-RYS12, (c) difference between the products. Area weighted mean seasonal temperature anomaly within the validation region: (d) CARIB12, (e) GLORYS12, (f) difference between the products.
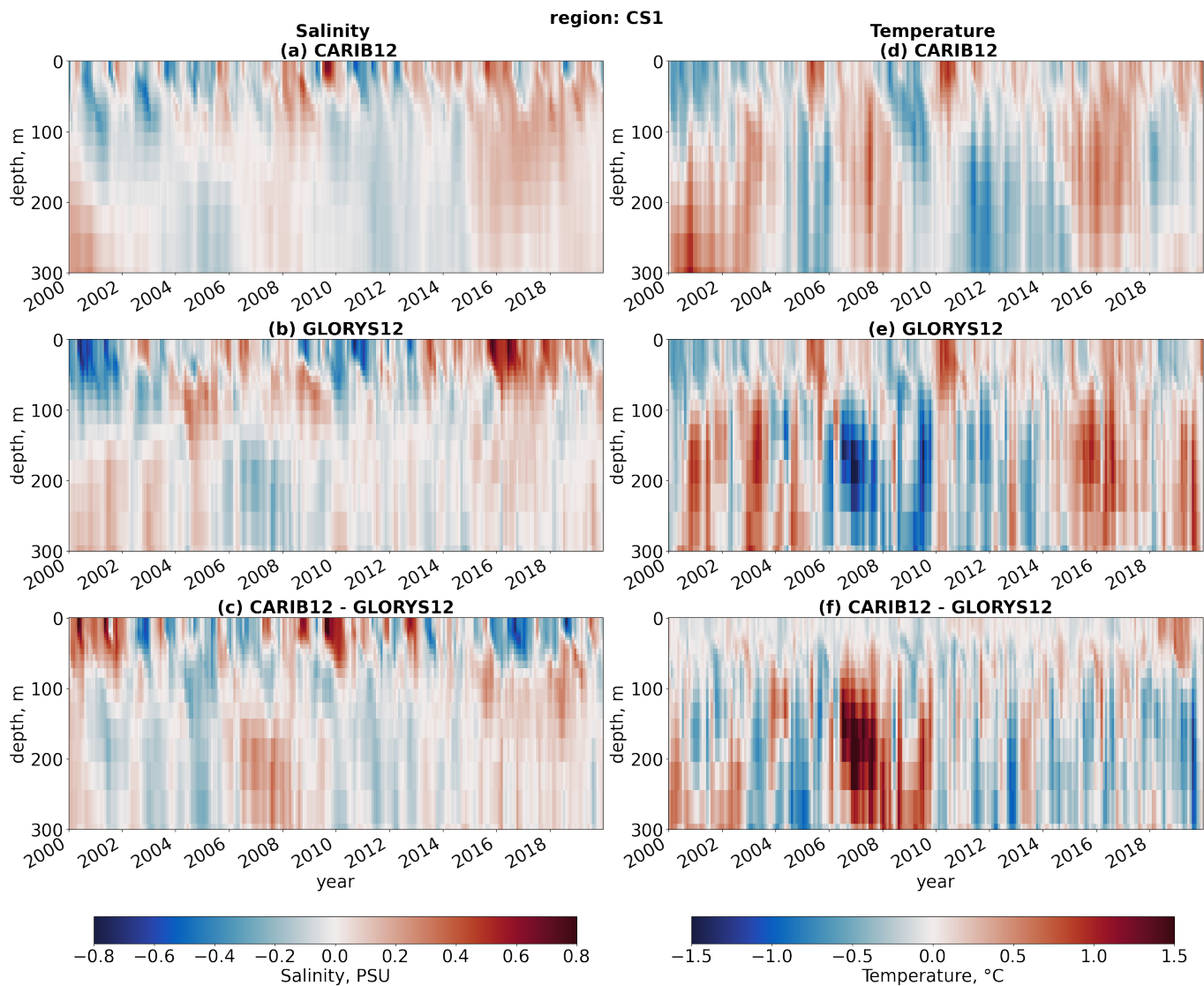
Figure 14. Area weighted mean monthly salinity anomaly within the CS (CS1 in Figure A5): (a) CARIB12, (b) GLORYS12, (c) difference between the products. Area weighted mean seasonal temperature anomaly within the validation region: (d) CARIB12, (e) GLORYS12, (f) difference between the products.
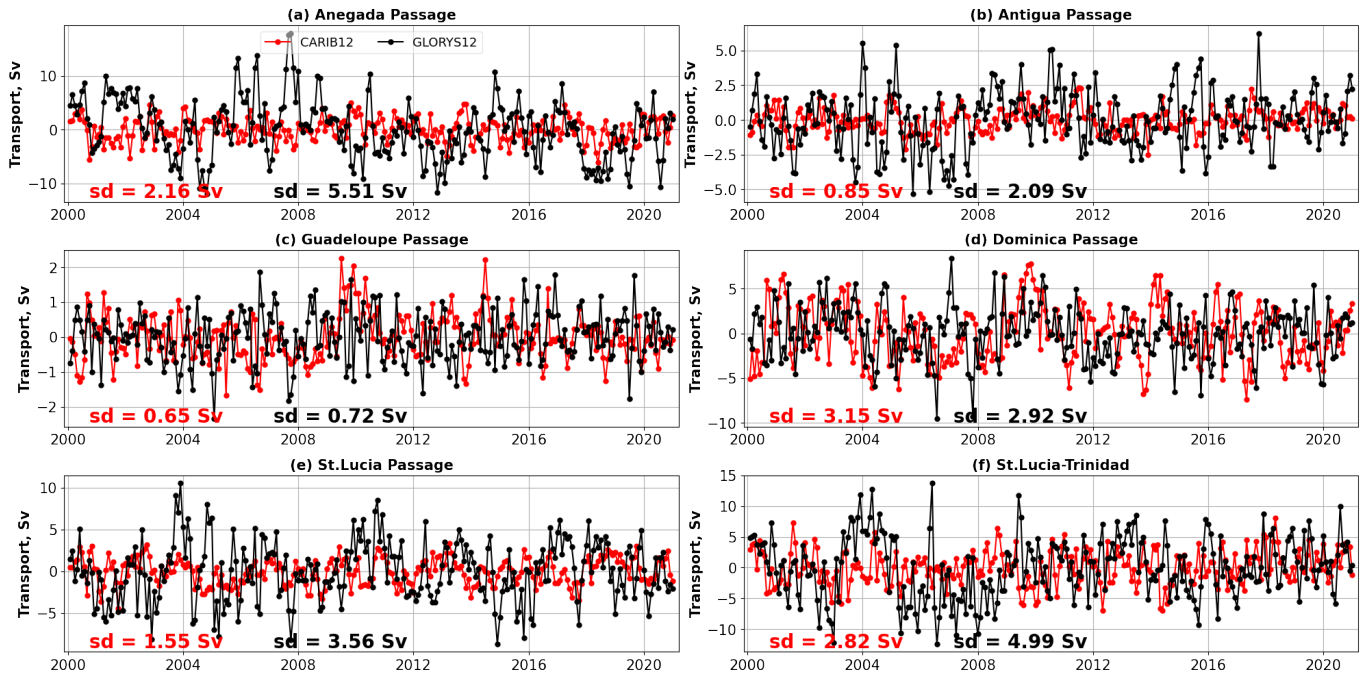
Figure 15. Transport through passages in the Eastern Caribbean Sea: monthly anomalies from CARIB12 (red) and GLORYS12 (black) for (a) Anegada Passage, (b) Antigua Passage, (c) Guadeloupe Passage, (d) Dominica Passage, (e) St. Lucia Passage and, (f) the St.Lucia - Trinidad transect. The standard deviation of the time series is indicated at the bottom of each panel, color coded by product. Time mean transports for each passage can be found in Table 4 for both CARIB12 and GLORYS12, as well as available observations.
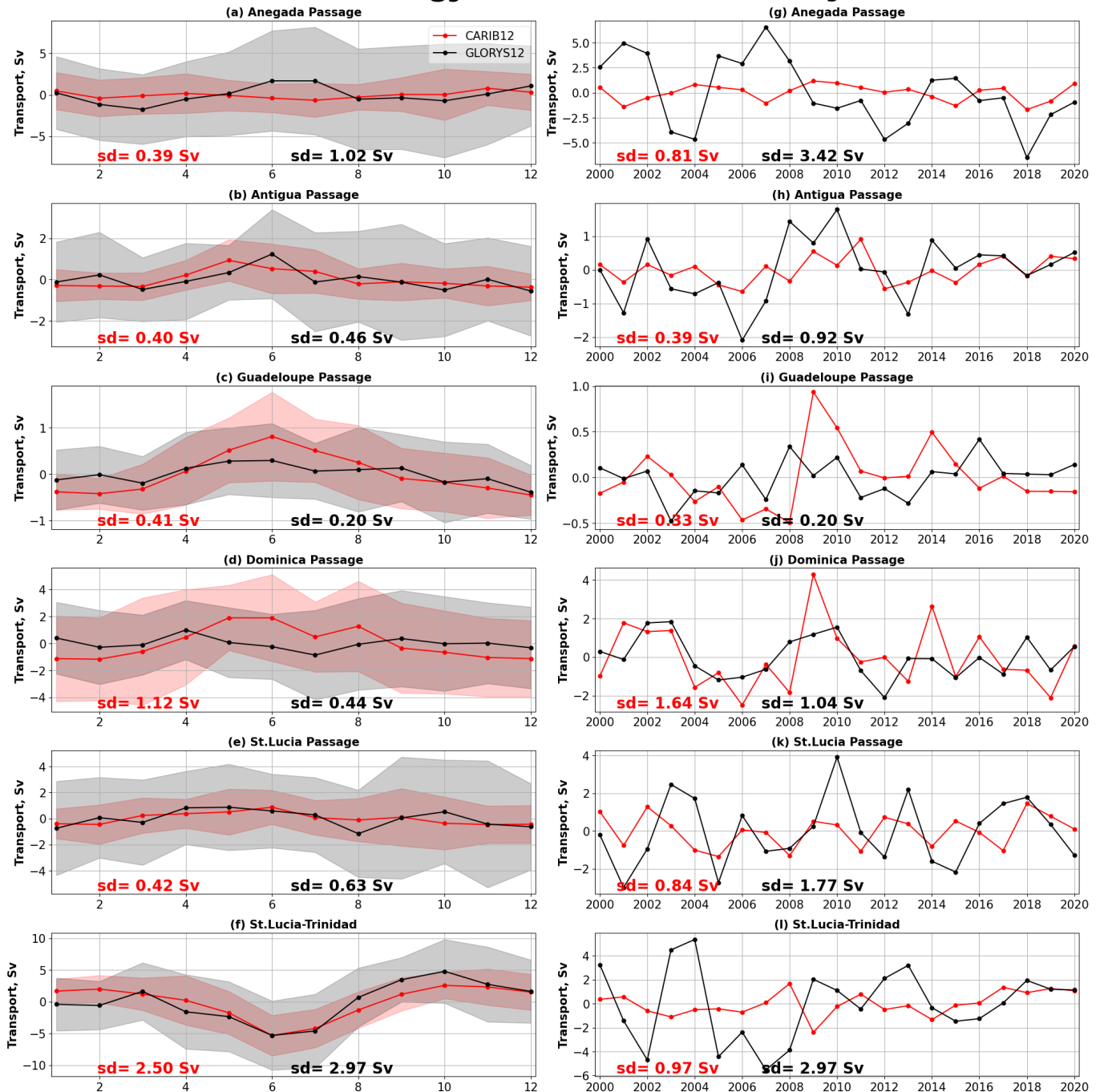
Figure 16. Transport through passages in the Eastern Caribbean Sea from CARIB12 (red) and GLORYS12 (black): (a-f) seasonal anomalies, and (g-l) yearly anomalies. In panels (a-f), the shading shows the standard deviation for each month (i.e. standard deviation of all January means, and so on).

700 **Appendix A: Supplemental Figures**
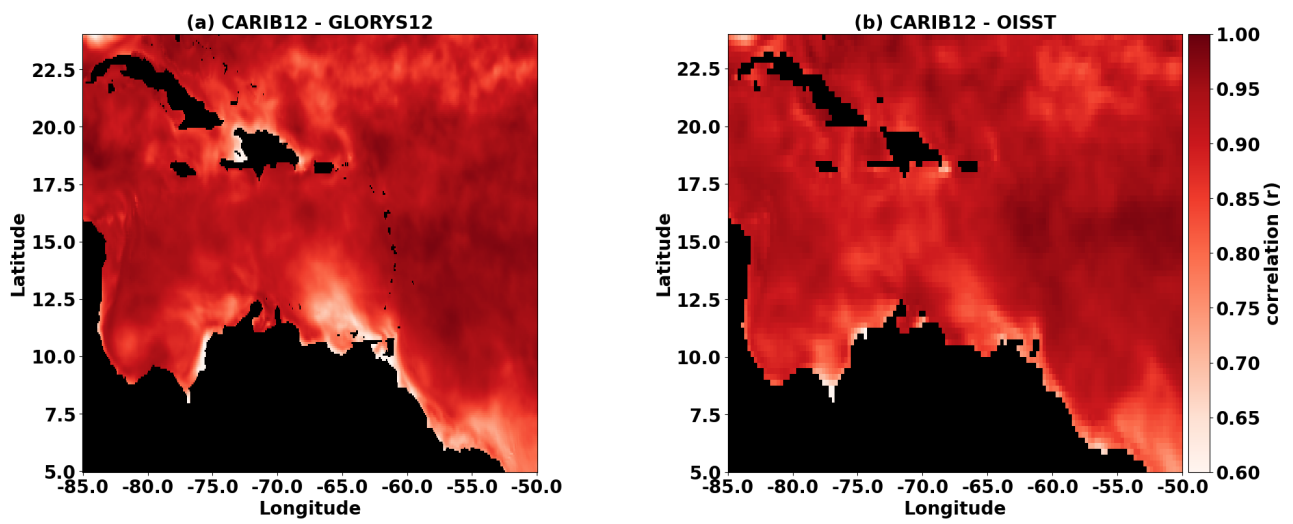
Figure A1. Correlation of the 12 month SST climatology between: (a) CARIB12 and GLORYS12, and (b) CARIB12 and OISST.
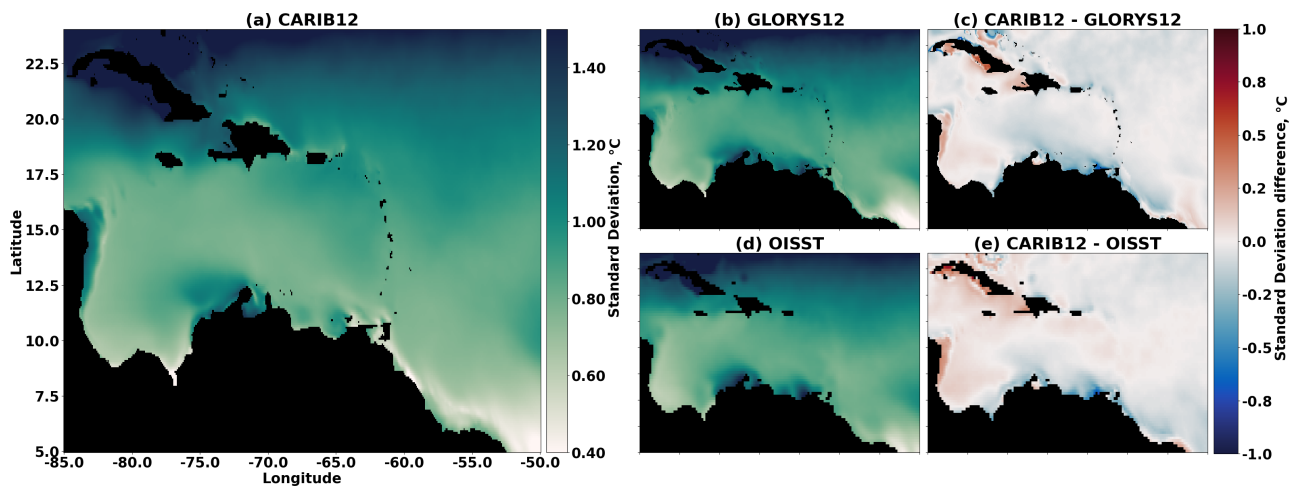
Figure A2. Standard deviation of the 12 month SST climatology from (a) CARIB12 (b) GLORYS12 (d) OISST. (c) Difference between the standard deviation of CARIB12 and GLORYS. (d) Difference between the standard deviations of CARIB12 and OISST.
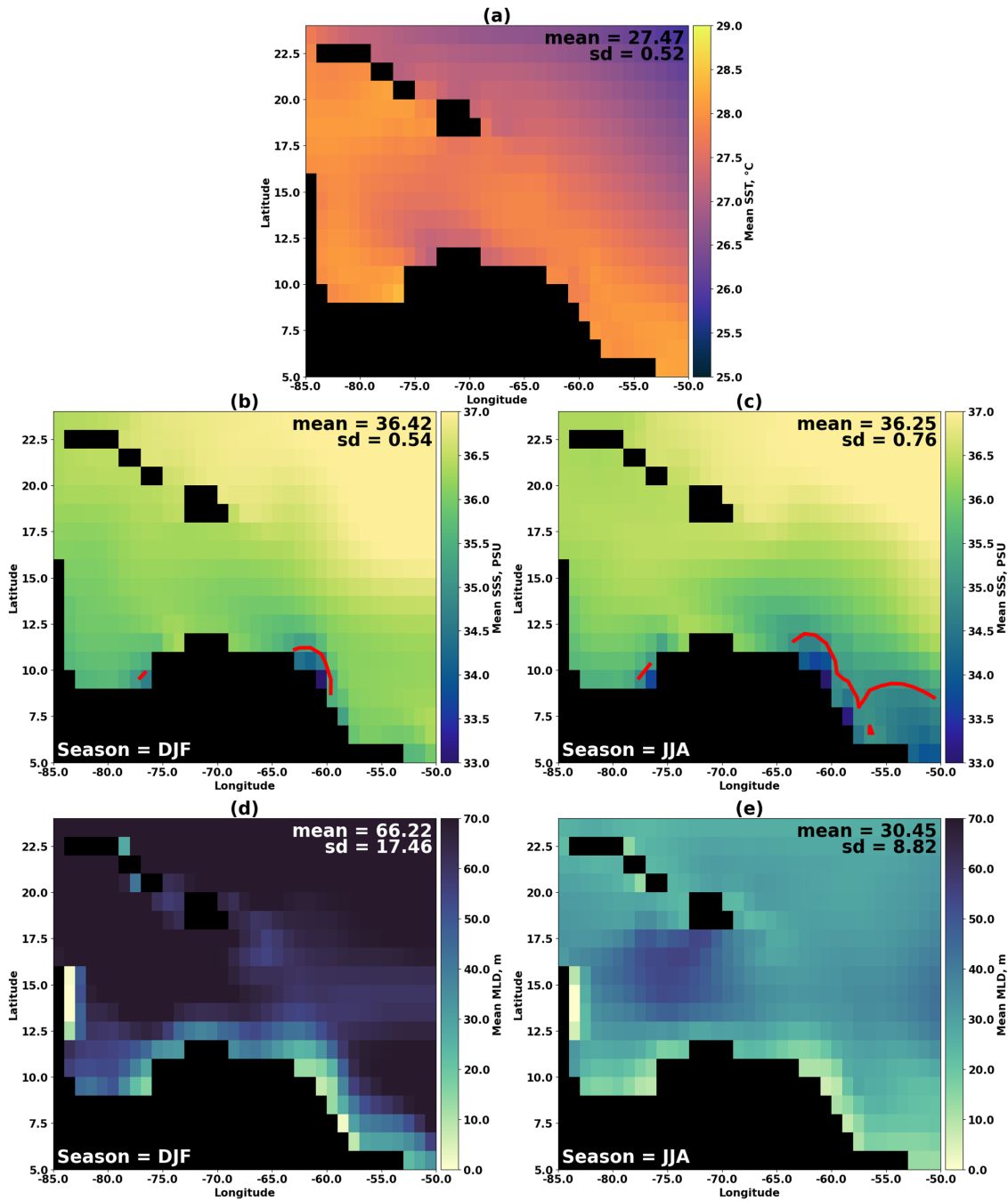
Figure A3. Mean fields and metrics for the $1°$ CESM-POP simulation within region of interest: (a) time mean SST (2000-2018), (b) winter time mean SSS (2000-2018), (c) summer time mean SSS (2000-2018), (d) winter time mean MLD (2000-2018), and (e) summer time mean MLD (2000-2018). The red line in (b) and (c) corresponds to the 35 PSU contour line. Spatial means and standard deviations are specified in the inset text for each panel.
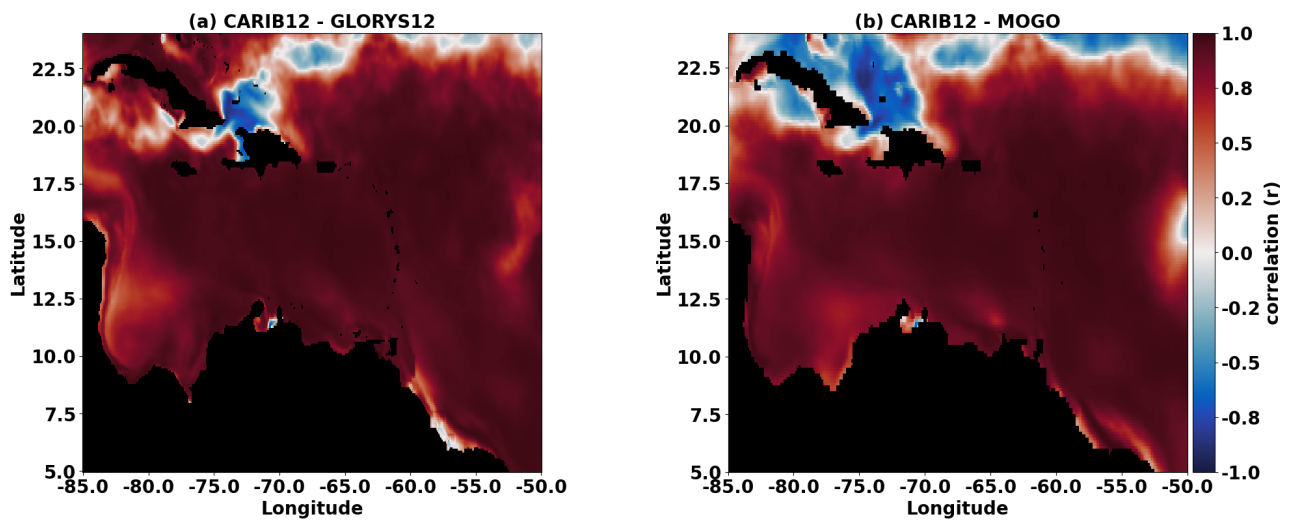
Figure A4. Correlation of the 12 month SSS climatology between: (a) CARIB12 and GLORYS12, and (b) CARIB12 and MOGO.
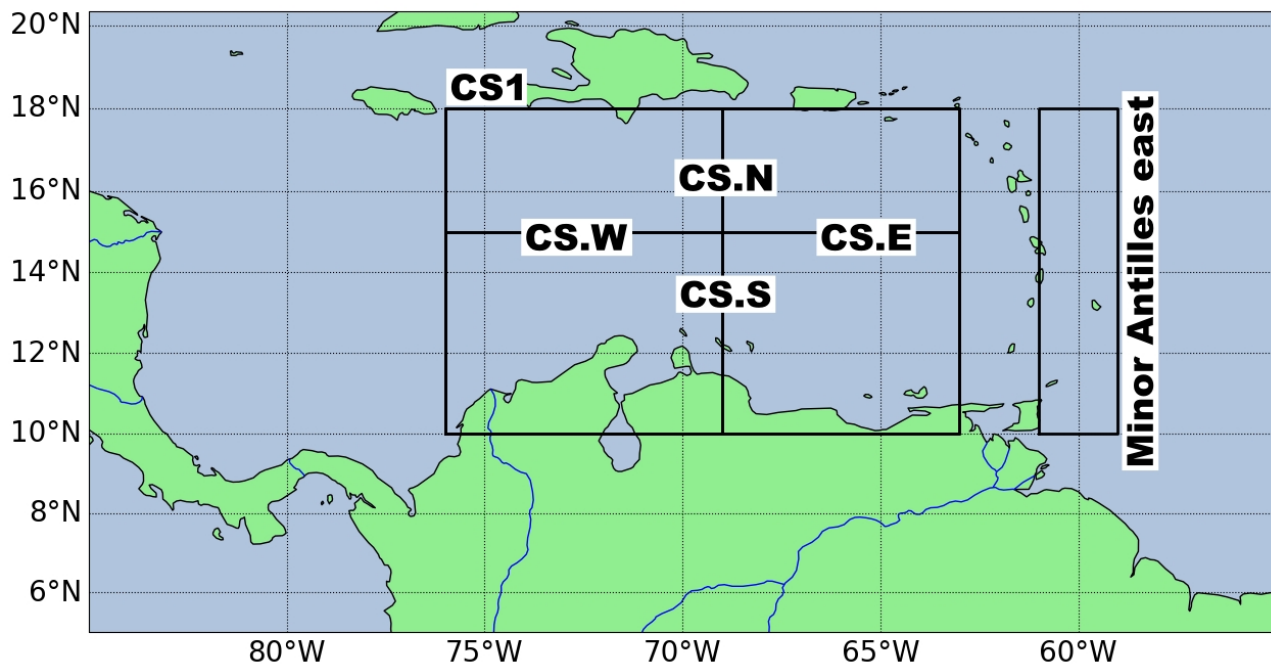
Figure A5. Sub-regions used for additional validation of CARIB12. Only validations for CS1, CS.E and Minor Antilles east are shown in addition to the the full validation region shown in Figure 1.
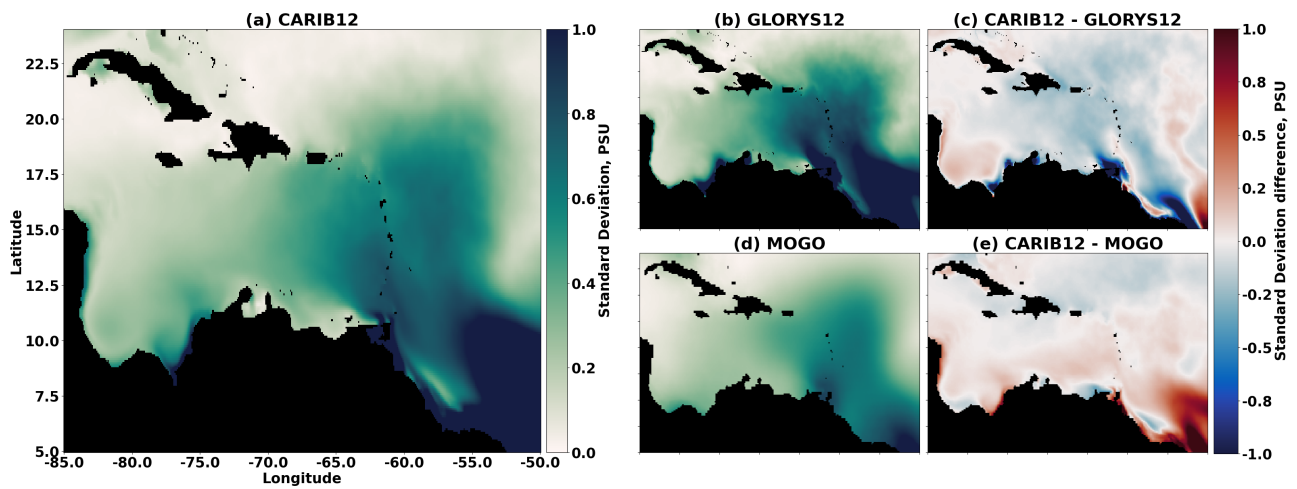
Figure A6. Standard deviation of the 12 month SSS climatology from (a) CARIB12 (b) GLORYS12 (d) MOGO. (c) Difference between the standard deviation of CARIB12 and GLORYS. (d) Difference between the standard deviations of CARIB12 and MOGO.

Appendix B: Representation of known Amazon river pathways into the Caribbean Sea in CARIB12

As described in Section 1, variability within the Caribbean Sea (CS) is closely linked to the influence of the Amazon and Orinoco river plumes. This includes control over near-surface salinity, stability of the Caribbean Current, the generation of mesoscale eddies and the modulation of the seasonal eddy kinetic energy across the CS (Chérubin and Richardson, 2007; Jouanno et al., 2012; Grodsky et al., 2015; Seijo-Ellis et al., 2023). A regional configuration of the CS, such as CARIB12, must properly capture the pathways and timing of plume waters entering the CS. We perform a case study validation of CARIB12 using the Lagrangian particle tracking model Ocean Parcels (Lange and Sebille, 2017; Delandmeter and Sebille, 2019). We replicate the methodology and experiment performed by Seijo-Ellis et al. (2023) to examine the origin and pathways of waters arriving to the Virgin Islands Basin (VIB). One hundred passive particles were released daily at the grid point closest to 18°N, 64.8°W; i.e. the closest point to site Bi14 in][]SEIJO2023 and backtracked for 100 days. Backtracking is done via a 4th order Runge-Kutta interpolation scheme using the CARIB12 daily surface velocity fields. This approach allows to trace the trajectories of the particles 100 days before their arrival to the release site. While we only show the year 2010 as an example (which also allows a comparison to the results shown in Figures 5 and 6 of Seijo-Ellis et al. (2023)) the backtracking was completed for the length of the simulation 2000-2020.

The analysis of the trajectories follows the same method described in Seijo-Ellis et al. (2023) and is summarized in Figure B1. For each arrival date (same as release date when backtracking), we count the number of trajectories within $0.2° \times 0.2°$ bins (Figure B1a). Two main constraints are enforced: particles with more than one position recorded in the same bin are only counted once, if a particle passes through but has no recorded position in a particular bin it is not counted. A probability density map of the trajectories of the particles 100 days prior to their release is then generated for each release date (Figure B1a and b). In order to summarize the temporal evolution of these binned trajectory maps, we generate a time series of the cumulative number of trajectories per bin color-coded by each bin's location (Figure B1c-e). The first step is to color code the bins by their location such that a change in color represents a meridional change in position, and a change in color shading represents a latitudinal change in position (Figure B1c). For each release date, color-coded bins are stacked on top of each other according to the number of particles in each bin and scaled according to the number of bins with particles (Figure B1d). The resulting time-series shows the pathways of waters arriving to the release site (Virgin Islands Basin) on any given date (Figure B1e). For a more detailed decription of the method please refer to Seijo-Ellis et al. (2023).

Salinity variability in the Virgin Islands Basin (VIB) is consistent with that of the wider Caribbean Sea and shows a strong seasonal component: salinity remains above 35.5 PSU during the first half of the year and below 35.5 PSU during the second half (Figure B2a, red line), consistent with the results for the wider CS in Sections 3.1 and 3.1.1. The black line in Figure B2a shows the near-surface salinity tendency ($\frac{\partial S}{\partial t}$, psu) and the blue line shows the near-surface horizontal salinity advection ($-u\frac{\partial S}{\partial x} - v\frac{\partial S}{\partial y}$, psu). The seasonal decrease in near-surface salinity (red line) is largely driven by the near-surface horizontal salinity advection (blue line) as that contributes to much of the change in the near-surface salinity tendency (black line). Variability in salinity advection is associated with intrusions of Amazon river waters: salinity starts decreasing between May and June, as Amazon river plume waters arrive into the VIB. The arrival of plume waters is indicated by the light blue colors

in Figure B2c) appearing around May in Figure B2c. The lack of light blue and green for most of the first half of the year indicate that waters arriving at the VIB were coming from the dark black, purple and red regions in Figure B2b. That agrees with previous studies showing that during winter and early spring, waters arriving at the VIB are saltier and slower moving than those during the second half of the year when near-surface horizontal advection is stronger (Figure B2a). During the second half of the year, when advection is stronger and more variable (e.g. September - October, 2010) waters arriving at the VIB followed a path from the Amazon river delta (light blue) northwestward along the shelf of South America (light green, orange and red) into the Caribbean Sea (light to medium purple) and to the release site in the VIB (blacks). Results here are consistent with findings by Seijo-Ellis et al. (2023) regarding the seasonality of salinity and the arrival of plume events in the VIB, and how near-surface horizontal advection plays a dominant role in the salt budget of the VIB. The consistency between the results here and those shown in Seijo-Ellis et al. (2023) is important as it shows that CARIB12 can replicate known pathways and variability of waters arriving at the VIB when compared to a data assimilating model such as the GLORYS reanalysis used in Seijo-Ellis et al. (2023). In particular, these results show that CARIB12 reproduces known patterns of near-surface horizontal advection which are important to study additional processes in the CS.
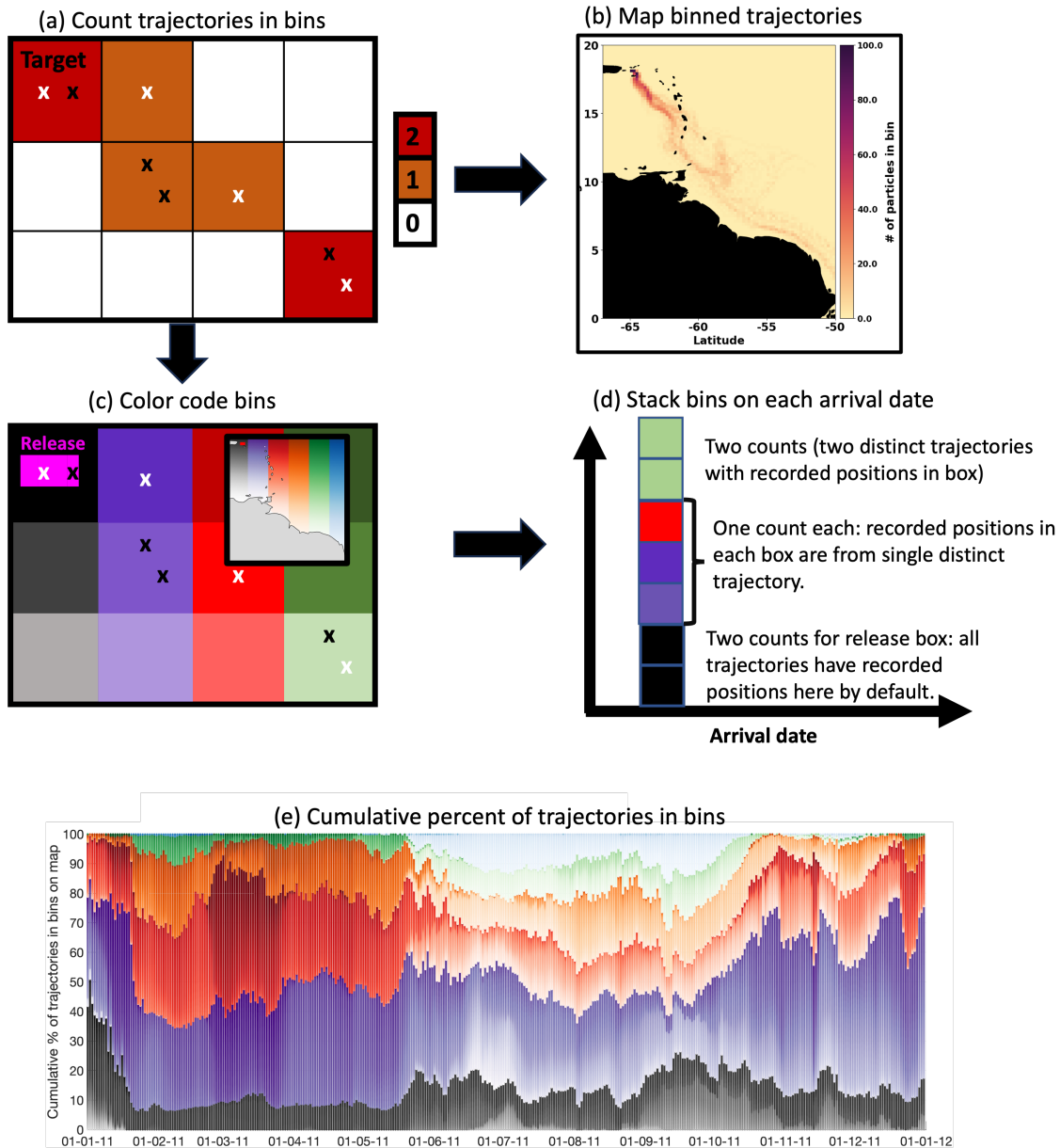
Figure B1. Schematic demonstrating the method used to generate Figures B2. a) Example positions of a trajectory for two particles (one black and one white). The 'Release' bin corresponds to the release site from which particles are backtracked. Positions within $0.2° \times 0.2°$ bins are counted and mapped as shown in panel (b). (c) Bins are now color-coded by their location (actual example in the inset map). A change in color represents a meridional position change, while a change in shading corresponds to a latitudinal position change. b) Example of position counting in each bin. (d) Example schematic of how the time series is generated. For each arrival date bins are stacked by the number of particles in each bin (scaled by the number of bins with recorded particles). (e) Actual example of the time series. The colored bins stacked on top of each day in the x-axis represent the pathway the waters came from. The inset map in panel (c) shows the color-coded bins to identify pathways. For a detailed description refer to Seijo-Ellis et al. (2023).
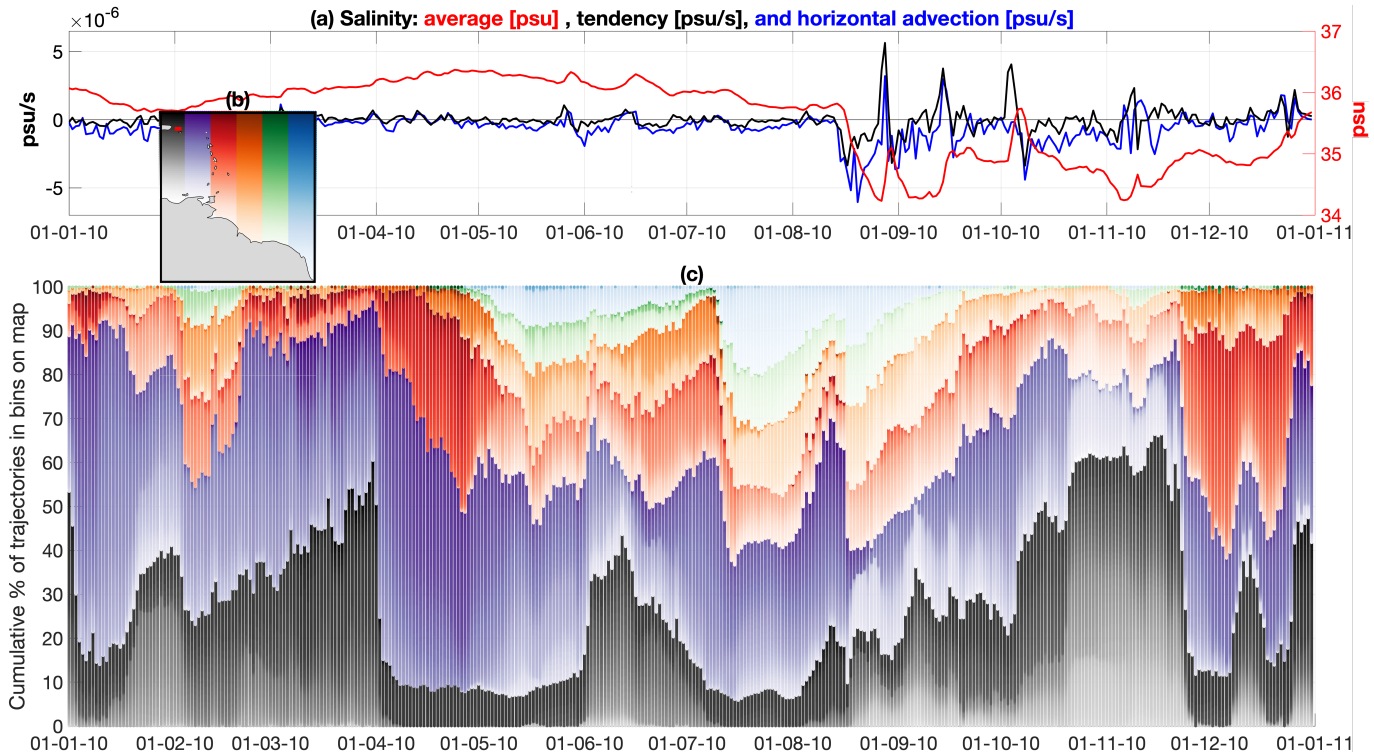
Figure B2. (a) Time series of SSS (red, right vertical axis), horizontal SSS advection (blue, left vertical axis) and SSS tendency (black, left vertical axis) within the VIB during 2010. (b) Map with color-coded bins used to identify the path of trajectories in panel (c). A change in bin color denotes a change in longitude and a change in shade (from light to dark) represents a change in latitude (from south to north). (c) Time series of cumulative percent of trajectories in bin: for each particle release date (i.e., for each arrival date into the region of interest, as we are backtracking) we stacked bins following the description in Seijo-Ellis et al. (2023). Bin colors indicate bin locations and correspond to the color distribution in panel (b). As an example, a high cumulative percent of trajectories in light colored bins (red through blue) indicates that particles arrived to the VIB from the south-west, along a path close the coast of South America.